REPORT 1093-29

REPORT

by

THE OHIO STATE UNIVERSITY RESEARCH FOUNDATION
COLUMBUS, OHIO 43212

Sponsor	National Aeronautics and Space Administration Office of Grants and Research Contracts Washington, D. C. 20546
Grant Number	NsG-74-60
Investigation of	Receiver Techniques and Detectors for Use at Millimeter and Submillimeter Wave Lengths
Subject of Report	Absorption in the Submillimeter Range
Submitted by	B. J. Lin Antenna Laboratory Department of Electrical Engineering
Date	15 December 1965

The material contained in this report is also used as a thesis submitted to the Department of Electrical Engineering, The Ohio State University as partial fulfillment for the degree of Master of Science.

ABSTRACT

Water-vapor absorption is the most intense absorption in the submillimeter region. With a new spectrometer, the Michelson type interferometer, investigation of absorption can be extended to a lower frequency range with better resolution and accuracy. An experimental setup is described which measures the water-vapor absorption from ν = 10 cm^{-1} to ν = 200 cm^{-1} at a pathlength of 200 ft. and pressures of 4.4 mm Hg and 1.1 mm Hg. Theories of the water-vapor rotational line positions are reviewed. A newly constructed high temperature submillimeter source is also described.

Author

ACKNOWLEDGMENTS

The author feels most indebted to Dr. R. A. Williams for his patient guidance and assistance throughout the investigation. The many helpful comments of Dr. R. K. Long and the assistance of Dr. William S. C. Chang, my former adviser, in helping to design the experiment and checking the second chapter of the thesis are very much appreciated.

CONTENTS

CHAPTER I
INTRODUCTION

The success of communication at submillimeter wavelengths depends greatly upon the intensity of the source, the absorption (i. e., attenuation) and scattering by the atmosphere, and the sensitivity of the detector. Absorption by the atmosphere is most commonly caused by the induced molecular absorption. Since electronic transitions occur mostly at visible and ultraviolet wavelengths and vibrational transitions occur mostly in visible and near infra-red wavelengths, the only kind of absorption that occurs in the submillimeter wavelengths is that caused by rotational transitions. In the atmosphere, only H_2O, O_2, N_2O, NO_2, CO, O_3, and SO_2 have a rotational spectrum since other atmospheric gases such as N_2 and H_2 do not have an electric or magnetic dipole moment to absorb electromagnetic radiation rotationally. Among the above mentioned absorbers, H_2O and O_2 are present in the largest concentration. O_2 has only one strong line at $\lambda \doteq 1/2$ cm. [1] On the other hand, the water-vapor rotational absorption spectrum is very intense and complex in the submillimeter wave region and is, therefore, of great importance.

The water-vapor rotational spectrum problem has been dealt with by many people both theoretically and experimentally. The most helpful theoretical work will be organized and presented in the next chapter. Most of the past experimental work was done with conventional grating spectrometers which have a low resolving power in this wavelength region and have a high low-frequency limit. For example, well-known work of Randall, Dennison, Ginsburg, and Weber [2] on the water-vapor rotational spectrum was done with a grating-type instrument having a resolving power of 0.5 cm^{-1} and an accuracy of 5% under optimum conditions. Its range is from 70 cm^{-1} to 560 cm^{-1}.

After the invention of the interferometric spectrometer [3, 4] it became possible to obtain much higher resolution and accuracy and to extend the measurements to lower frequencies. For example, the interferometer that was used for this study currently has a maximum resolving power of 0.25 cm^{-1} with an accuracy, under optimum conditions, of 0.04% of the wavenumber of the absorption line being observed; its range is from 10 cm^{-1} to 200 cm^{-1}. Chapter III gives a more detailed discussion of this instrument. Therefore, it is worthwhile to study further the submillimeter water-vapor spectrum with the new instrument. The purpose of the present work is to describe a setup for these experiments.

More extensive measurements will be conducted after the success of these techniques is demonstrated.

It is difficult to obtain a satisfactory signal-to-noise ratio in submillimeter experiments because of the relatively weak sources and insensitive detectors available in this region. The experiment to be described uses a helium-cooled Germanium bolometer detector [5] and an intense 2500°K black-body source of new design to achieve an improved signal-to-noise ratio. A 50-foot multi-traversal absorption cell suitable for low pressure long pathlength measurement was used to avoid pressure-broadening effects.

In the following sections, the theories used to obtain the position of the rotational spectral lines are summarized and a table of predicted line positions for H_2O is presented. The components of the experimental setup are then illustrated and discussed. Finally, the results of the absorption measurements are shown with interpretation and discussion.

CHAPTER II
THEORY OF SUBMILLIMETER ROTATIONAL ABSORPTION BY WATER-VAPOR

A. General Discussion

To calculate the position of the absorption lines of a certain medium, it is necessary to know its energy levels and the selection rule governing transition of these levels. Energy levels are obtained quantum mechanically by solving the equation $H\psi = E\psi$. The selection rules are obtained by considering symmetries that will make μ_g the matrix element of the transition zero. To solve the equation $H\psi = E\psi$, the explicit expression of the Hamiltonian must be known. In the water-vapor case, H turns out to be very

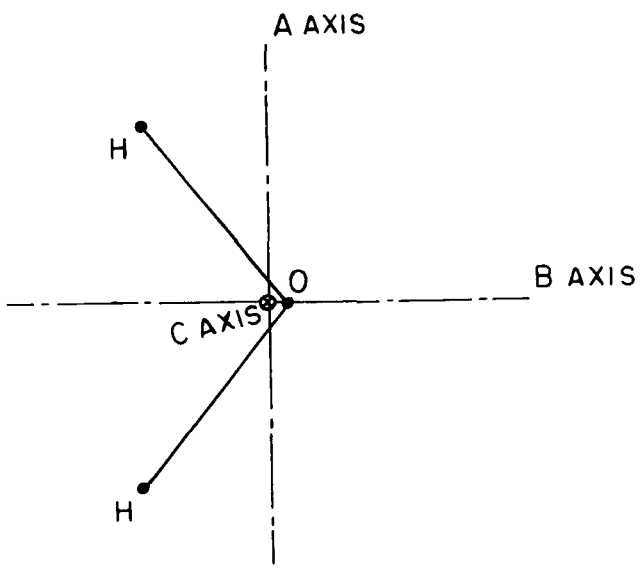

Fig. 1. The water-vapor molecule.

complicated [6] because the three principal moments of intertia of the water-vapor molecule (i.e., $I_A = 1.0066 \times 10^{-40}$ gm - cm^2, $I_B = 1.93066 \times 10^{-40}$ gm - cm^2, and $I_C = 3.01631 \times 10^{-40}$ gm - cm^2) are very different. [2] The problem can be best approached by solving for the energy levels of an asymmetric rotor. At high rotational energy, centrifugal distortion plays a very significant part and must be taken into account.

Section B will summarize the historical works on evaluation of the energy levels of an asymmetric rotor. Section C will discuss the selection rules and derive the selection rules of the water-vapor molecule. Section D will give a table of water-vapor absorption lines from 10 cm^{-1} to 70 cm^{-1}.

B. Determination of Energy Levels of an Asymmetric Rotor

Kramers and Ittmann [7, 8, 9] were the first to solve the asymmetric rotor problem. Dennison [10] extended the method and Wang [6] gave the most general result for the energy of an asymmetric rotor:

$$E = \frac{h^2 c}{8\pi^2} [a J(J+1) + \omega], \tag{1}$$

where c is defined as in Eq. (2), J is the quantum number of angular momentum, and ω is one of the $2J+1$ roots of the following secular determinant of degree $2J+1$:

$$
(2) \qquad \begin{vmatrix}
J^2-\omega \cdots & & & & \\
 & 0 & bf(J,1) & 0 & \\
 & 1^2-\omega & 0 & bf(J,0) & \\
 & 0 & 0^2-\omega & 0 & \\
 & bf(J,0) & 0 & (-1)^2-\omega & \\
 & 0 & bf(J,-1) & 0 & \\
 & & & & \ddots \\
 & & & & J^2-\omega
\end{vmatrix} = 0,
$$

where

$$
f(J,K) = -\frac{1}{2}\left[(J-K)(J-K+1)(J+K)(J+K+1)\right]^{\frac{1}{2}},
$$

$$
c = \frac{1}{A_z} - \frac{1}{2}\left(\frac{1}{A_x} + \frac{1}{A_z}\right),
$$

$$
a = \frac{1}{2c}\left(\frac{1}{A_x} + \frac{1}{A_y}\right),
$$

$$
b = \frac{1}{2c}\left(\frac{1}{A_x} - \frac{1}{A_y}\right),
$$

and A_x, A_y, A_z are the three principal moments of inertia of the rotor.

The only necessary restriction leading to Wang's result was $A_x < A_y < A_z$ or $A_x > A_y > A_z$, which means $-1 \leq b \leq 0$.

To solve the secular determinant, Randall, Dennison, Ginsburg, and Weber expanded it into a $2(J+1)$ degree polynomial for $J = 0$ up to $J = 11$.[2, 11] For example, the equation for $J = 0$, is $\omega = 0$; for $J = 1$, it is $\omega(\omega-1-b)(\omega-1+b) = 0$; and for $J = 2$, $(\omega-4)(\omega-1+3b)(\omega-1-3b)(\omega^2-4\omega-12b^2) = 0$ is obtained. The roots of the ω's can be

found readily from these algebraic equations and the substitution of these roots into Eq. (1) will give the energy levels. It is customary to label the $2J+1$ different energy levels in increasing order by an integer which ranges from $-J$, to $-J+1, \cdots +J$. Then, each energy level is denoted by E_{τ}^{J}.

The quantum number of the energy state J_{τ} is also represented by $J_{K_{-1}K_1}$, where K_{-1} is the largest quantum number of the z-axis component of angular momentum J of the limiting prolate top. The reason for such an equivalent representation is explained as follows.

A good way to denote the asymmetry is to use the asymmetric parameter $\kappa = \frac{2B-A-C}{A-C}$, where $A = \frac{h^2}{2I_A}$, $B = \frac{h^2}{2I_B}$, $C = \frac{h^2}{2I_C}$, and $I_A \leq I_B \leq I_C$. When the rotor becomes a prolate top, i.e., $I_B = I_C$, κ becomes -1; when the rotor becomes an oblate top, i.e., $I_A = I_B$, κ becomes 1; when the rotor is asymmetric κ ranges between -1 and 1. If one draws the energy levels of asymmetric rotors of different asymmetry, i.e., with different values of κ as shown in Fig. 2, we notice that the two-fold degeneracy of the prolate top rotor and the two-fold degeneracy of the oblate-top rotor split into two non-degenerate energy levels as the rotor deviates from being a symmetric top. Labeling the asymmetric levels by J_{τ} in increasing order of magnitude we notice that $\tau = K_{-1} - K_1$;

τ and $K_{-1}K_1$ are one-to-one in correspondence. Indeed, the $J_{K_{-1}K_1}$ way gives a clearer view of the symmetric property of the rotor which will be presented in the next section.

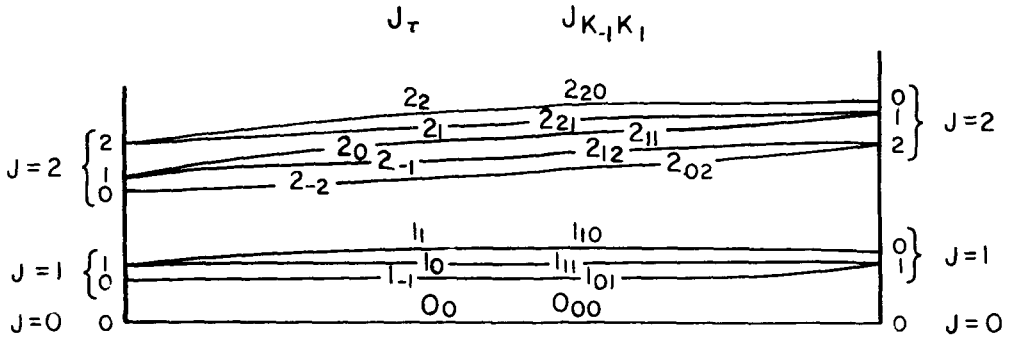

Fig. 2. Qualitative energy level splitting due to asymmetry.

Wang's secular determinant method is a very general method but every time a different molecule is investigated those high degree polynomials must be solved tediously. King, Hainer, and Cross [12] introduced a method in which the tedious calculations are performed once and for all; changing the kind of molecule only changes certain parameters in an algebraic equation. In that method, they equated the J_τ energy level of an arbitrarily shaped rotor to the J_τ universal energy level which has been tabulatedas a function of K which gives

(3) $$E_{\tau}^{J}(A, B, C) = \frac{A-C}{2} E_{\tau}^{J}(K) + \frac{A+C}{2} J(J+1) .$$

$E_{\tau}^{J}(K)$ was tabulated from K = -1 to 0 at 0.1 intervals; J from 0 to 10. The values of $E_{\tau}^{J}(K)$ from 0 to 1 can be obtained from the following equation:

(4) $$E_{\tau}^{J}(K) = -E_{-\tau}(-K) .$$

Schwendeman, [13] Polo, [14] Brown and Parker, [15] and Baker [16] gave modifications to the preceding two methods. Energy levels as high as J = 40 have been calculated.

C. Selection Rules of Resonance Transitions

Merely knowing the energy levels is sufficient to construct the transition line positions, but many lines with zero transition intensity will be constructed. It is desirable to rule out this kind of transition with selection rules. The selection rules, obtained from this symmetric property of the wavefunction, turn out to be dependent on the orientation of the dipole moment in the molecule.

The symmetric property of the energy eigenfunction $\psi_{JK_{-1}K_1M}$ of an asymmetric rotor is summarized in Table I [20]

TABLE I

K_{-1}	K_1	C_2^A	C_2^B	C_2^C
+	+	+	+	+
-	+	+	-	-
-	-	-	+	-
+	-	-	-	-

where J is the quantum number of the total angular momentum; K_{-1}, K_1 are the quantum numbers mentioned in Section B; M is the quantum number of the z-component of the total angular momentum; (+) denotes evenness of ψ; and (-) denotes oddness of ψ. C_2^A is the transformation of a rotation of 180° about A. In this transformation $\theta \rightarrow (\pi - \theta')$. The Euler's angles that describe the rotation of the molecule become $\phi \rightarrow (\pi - \phi')$, and $\psi \rightarrow (\pi + \psi')$. C_2^B is the transformation of the rotation 180° about B and the Euler's angles become $\theta \rightarrow (\pi - \theta')$, $\phi \rightarrow (2\pi - \phi')$, and $\psi \rightarrow (\pi + \psi')$. C_2^C is the transformation of the rotation 180° about C and the Euler's angles become $\theta \rightarrow (\theta')$, $\phi \rightarrow (\pi + \phi')$, and $\psi \rightarrow (\psi')$.

The intensity of transition for state 1 to state 2 is proportional to the matrix element of the transition given by

$$\mu_g = \int_0^{\pi} \int_0^{2\pi} \int_0^{2\pi} \psi^*_{J_1 \tau_1 M_1} (\vec{\mu} \cdot \hat{g}) \psi_{J_2 \tau_2 M_2} \sin\theta \, d\theta \, d\phi \, d\psi. \tag{5}$$

The relation $\mu_g = 0$ implies that no transition will occur.

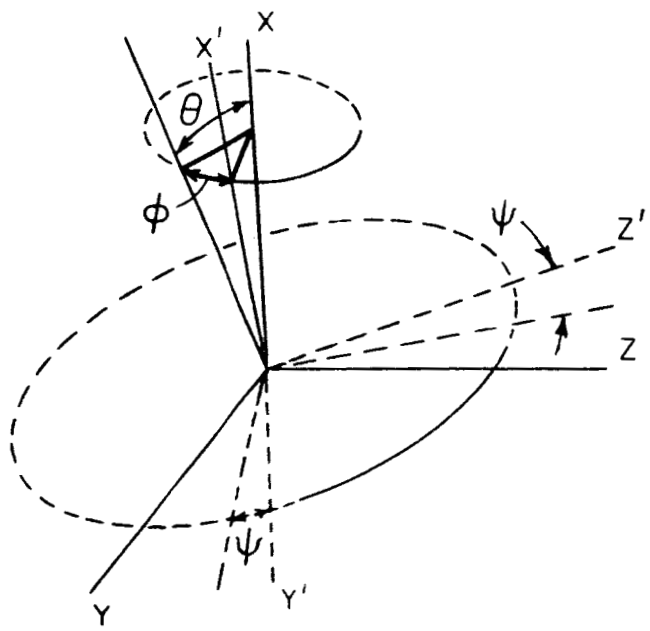

Fig. 3. Euler's angles.

The zero intensity transition of the water vapor molecule can be explained in the following manner: The electric dipole of the water vapor molecule lies along B, i. e. $\mu = \mu_B$. If the transformation C_2^A is performed, $(\vec{\mu} \cdot \hat{g}) \rightarrow -(\vec{\mu} \cdot \hat{g})$, $\theta \rightarrow \pi - \theta$, $\phi \rightarrow \pi - \phi$, and $\psi \rightarrow \pi - \psi$, and the matrix element becomes

$$(6) \qquad \mu_g = \int_{\pi}^{o} \int_{\pi}^{-\pi} \int_{\pi}^{3\pi} (\psi'_{J_1 \tau_1 M_1})^* (-\vec{\mu} \cdot \hat{g}) (\psi'_{J_2 \tau_2 M_2}) \sin(\pi-\theta)\, d(\pi-\theta)\, d(\pi-\phi)\, d(\pi+\psi)$$

or

$$(7) \qquad \mu_g = -\int_0^{\pi}\int_{-\pi}^{\pi}\int_0^{2\pi} (\psi'_{J_1\tau_1M_1})^* (\vec{\mu}\cdot\hat{g})\,(\psi'_{J_2\tau_2M_2})$$

$$\sin\phi\, d\theta\, d\phi\, d\psi.$$

Note that μ_g should not change under this symmetric operation on the coordinates. If one equates the right-hand side of Eq. (7) with the right-hand side of Eq. (5), it is observed that

$$(8) \qquad (\psi'_{J_1\tau_1M_1})^* (\psi'_{J_2\tau_2M_2}) = -\psi^*_{J_1\tau_1M_1}\,\psi_{J_2\tau_2M_2} \quad ,$$

in order that $\mu_g \neq 0$; i.e., when ψ_1 is odd, ψ_2 has to be even, or when ψ_1 is even, ψ_2 has to be odd.

Similar consideration of the transformation C_2^C yields the non-zero μ_g criteria as ψ_1 odd, ψ_2 even; or ψ_1 even, ψ_2 odd. The transformation C_2^B preserves the polarity of $\vec{\mu}\cdot\hat{g}$ because $\vec{\mu}$ lies along $\vec{B}$. The non-zero μ_g criterion is, then, ψ_1 even, ψ_2 even; or ψ_1 odd, ψ_2 odd.

Using Table I and the preceding discussion, we conclude that the allowed transitions for the water-vapor molecule are as shown in Table II.

TABLE II

$K_{-1}K_1 \leftrightarrow$	$K_{-1}'\,K_1'$
+ +	$\leftrightarrow$ - -
+ -	$\leftrightarrow$ - +

D. Line Positions of Water-Vapor Absorption in the 10 cm^{-1} to 200^{-1} Range

Randall, Dennison, Ginsburg, and Weber [2] investigated the water-vapor spectrum from 74 cm^{-1} to 560 cm^{-1}. They compared the line positions which they obtained experimentally with the calculated line positions obtained from the calculated energy levels and the selection rules. By this comparison, they were able to determine the states that correspond to the transitions and to construct the empirical energy levels from J = 0 to J = 11, with only a very few exceptional energy levels which they could not determine empirically and for which they used the calculated values instead. These values are 1_{-1}, 1_0, 1_1, 2_{-2}, 2_0, 11_{-1}, and 11_{-2}.

Because of the extended lower frequency range of our proposed experiment, more line position estimations are needed to check the experimental result. They were calculated according to the selection rules with the energy levels of Randall, Dennison, Ginsburg, and Weber. [2] Thus, these lines are half theoretical and half empirical in nature but will serve the purpose of checking experimental results. These newly calculated line positions are listed in Table III as ν_R.

The desired region of our experiment will be from ν = 10 cm^{-1} to ν = 200 cm^{-1}. The line positions above 74 cm^{-1} and the experimental energy levels from J = 0 to J = 11 can be found in Randall, Dennison, Ginsburg and Weber's paper. [2]

TABLE III

Line Positions from ν = 0.74 cm^{-1} to ν = 76.70 cm^{-1}

$\nu_B(cm^{-1})$	$\nu_R(cm^{-1})$	J_T	$J'_{T'}$	$\nu_B(cm^{-1})$	$\nu_R(cm^{-1})$	J_T	$J'_{T'}$
0.74	0.68	6_{-5}	5_{-1}	40.51	40.48	9_2	8_6
6.11	6.07	3_{-2}	2_2	40.65	40.48	9_3	8_5
10.69	10.78	10_{-7}	9_{-3}	41.00	41.06	2_2	2_0
10.91	10.88	5_{-4}	4_0	42.62	42.65	7_1	6_3
12.67	12.67	4_{-3}	3_1	43.26	43.19	8_{-5}	7_{-1}
13.10	13.00	10_{-4}	11_{-8}	43.66	43.70	8_{-1}	9_{-7}
14.53	14.54	7_2	6_6	44.12	44.14	6_{-3}	5_1
14.64	14.60	6_1	5_5	44.65	44.37	10_3	9_7
14.74	14.73	7_3	6_5	44.65	44.37	10_4	9_6
14.94	14.88	4_{-1}	3_3	44.85	44.80	7_0	8_{-6}
15.69	15.54	6_2	5_4	47.05	47.07	5_{-1}	5_{-3}
15.81	15.70	5_0	4_4	47.85	47.49	9_{-2}	10_{-8}
16.24	16.25	6_{-2}	7_{-6}	48.02	47.91	7_{-4}	6_0
16.69	16.63	8_3	7_7		50.64	2_1	3_3
16.72	16.63	8_4	7_6	51.44	51.42	6_0	5_2
18.57	18.52	1_1	1_{-1}	52.54	52.50	6_1	7_{-5}
20.64	20.62	5_1	4_3	53.20	53.17	8_1	9_{-5}
	21.41	8_7	9_5	53.48	53.31	4_{-2}	4_{-4}
	21.41	8_8	9_4	55.43	55.43	2_1	2_{-1}
25.07	25.01	2_0	2_{-2}	55.69	55.60	2_{-1}	1_{-1}
28.17	28.62	10_{-1}	11_{-7}	56.53	56.52	10_{-3}	11_{-9}
	28.67	9_8	10_6	57.13	57.26	4_1	5_{-5}
	28.67	10_5	9_9	57.29	57.36	3_{-3}	2_{-1}
30.21	27.80	9_{-6}	8_{-2}	57.32	57.25	5_0	6_{-6}
30.48	30.40	4_0	3_2	58.88	58.94	7_{-2}	6_2
32.35	32.12	5_{-2}	4_2	58.89	58.85	6_0	6_{-2}
32.95	32.97	2_{-2}	1_0	59.80	59.98	6_{-2}	6_{-4}
36.59	36.59	3_{-1}	3_{-3}	59.95	60.11	7_{-1}	7_{-3}
37.13	37.06	0_0	1_0	61.60	64.47	10_1	11_{-5}
	38.14	10_{10}	11_6	62.30	62.34	5_1	5_{-1}
	38.14	10_9	11_7	62.69	62.79	6_{-1}	7_{-7}
38.20	38.23	7_{-3}	8_{-7}	62.70	62.81	8_{-4}	9_{-8}
38.45	38.52	3_{-1}	2_1	62.95	63.04	8_{-1}	7_3
38.63	38.69	6_{-1}	5_3	63.21	63.36	3_2	4_{-4}
38.80	38.74	3_1	3_{-1}	63.44		12_{-7}	11_{-3}
39.00	38.82	8_1	7_5	63.44	63.57	9_0	8_4
39.11	39.03	7_0	6_4	64.01	64.03	5_{-1}	4_1
39.72	39.61	8_2	7_4	64.02	64.08	3_0	3_{-2}
40.21	40.45	4_0	4_{-2}	64.42	64.50	10_1	9_5

TABLE III (Continued)

$\nu_B(cm^{-1})$	$\nu_R(cm^{-1})$	J_τ	$J'_{\tau'}$	$\nu_B(cm^{-1})$	$\nu_R(cm^{-1})$	J_τ	$J'_{\tau'}$
64.95	64.98	10_2	9_4	72.18	72.14	3_{-2}	2_{-2}
65.82	65.89	9_1	8_3		72.22	7_2	8_0
67.25	67.41	5_2	6_{-4}	72.56	72.54	7_{-2}	8_{-8}
67.28	69.70	8_{-2}	8_{-4}	73.24	73.38	3_3	3_1
67.55	67.69	11_2	10_6	74.09	74.22	5_{-2}	5_{-5}
67.60	67.74	11_3	10_5	74.91	74.88	8_{-3}	7_1
68.10	68.24	4_2	4_0	75.51	75.59	4_{-1}	4_{-3}
69.24	68.96	4_{-2}	3_0	76.70	76.66	7_2	8_{-4}

A table of water-vapor line positions, line strengths, and line widths was obtained from Dr. Benedict along with his permission to use it. In the region 10 cm^{-1} to 74 cm^{-1} Benedict's values are listed in the table as ν_B. A plot of theoretical line positions and strengths from his table is shown in Fig. 4.

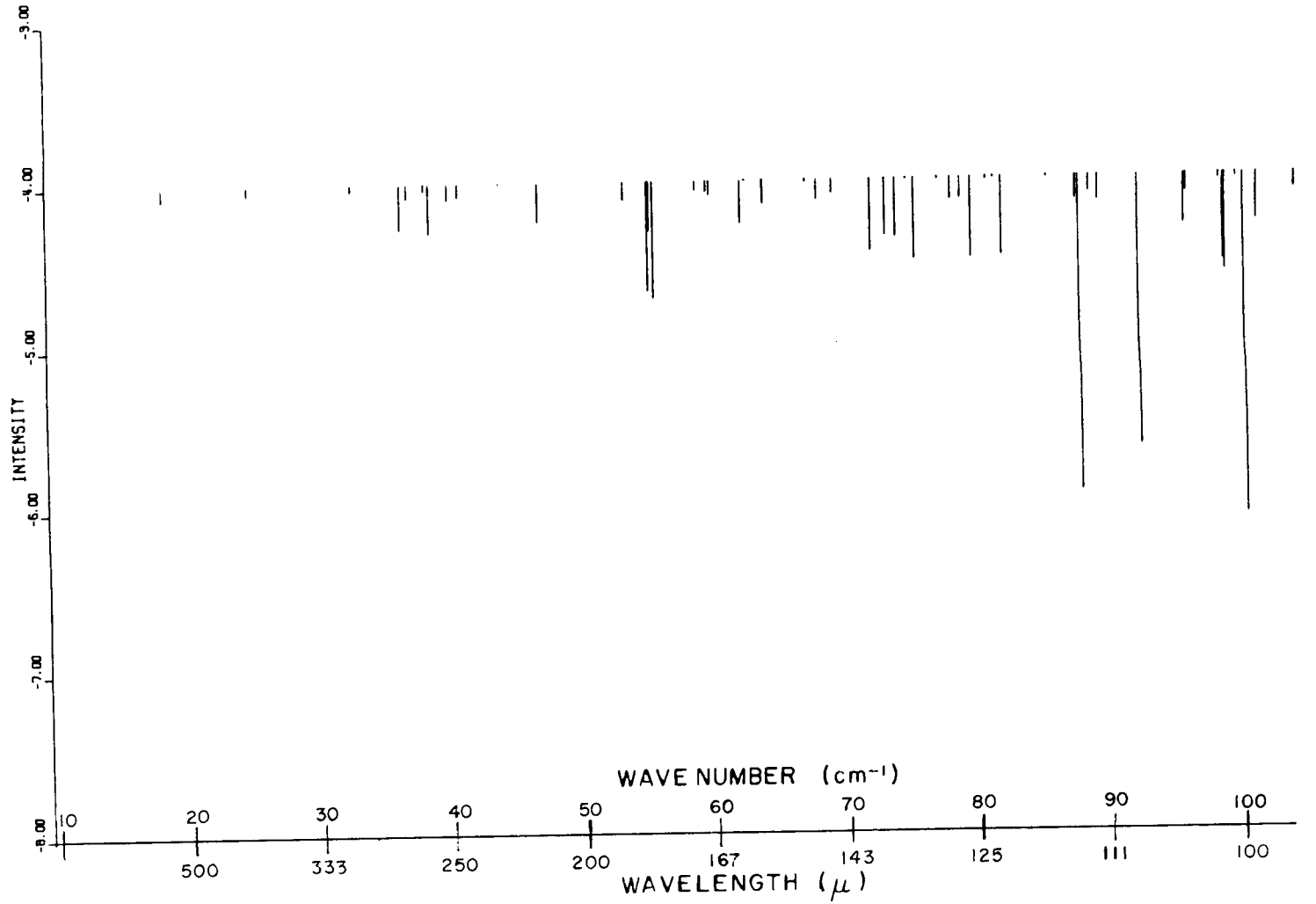

Fig. 4. A plot of Benedict's theoretical line positions and intensities from $\nu = 10\ cm^{-1}$ to $\nu = 200\ cm^{-1}$.

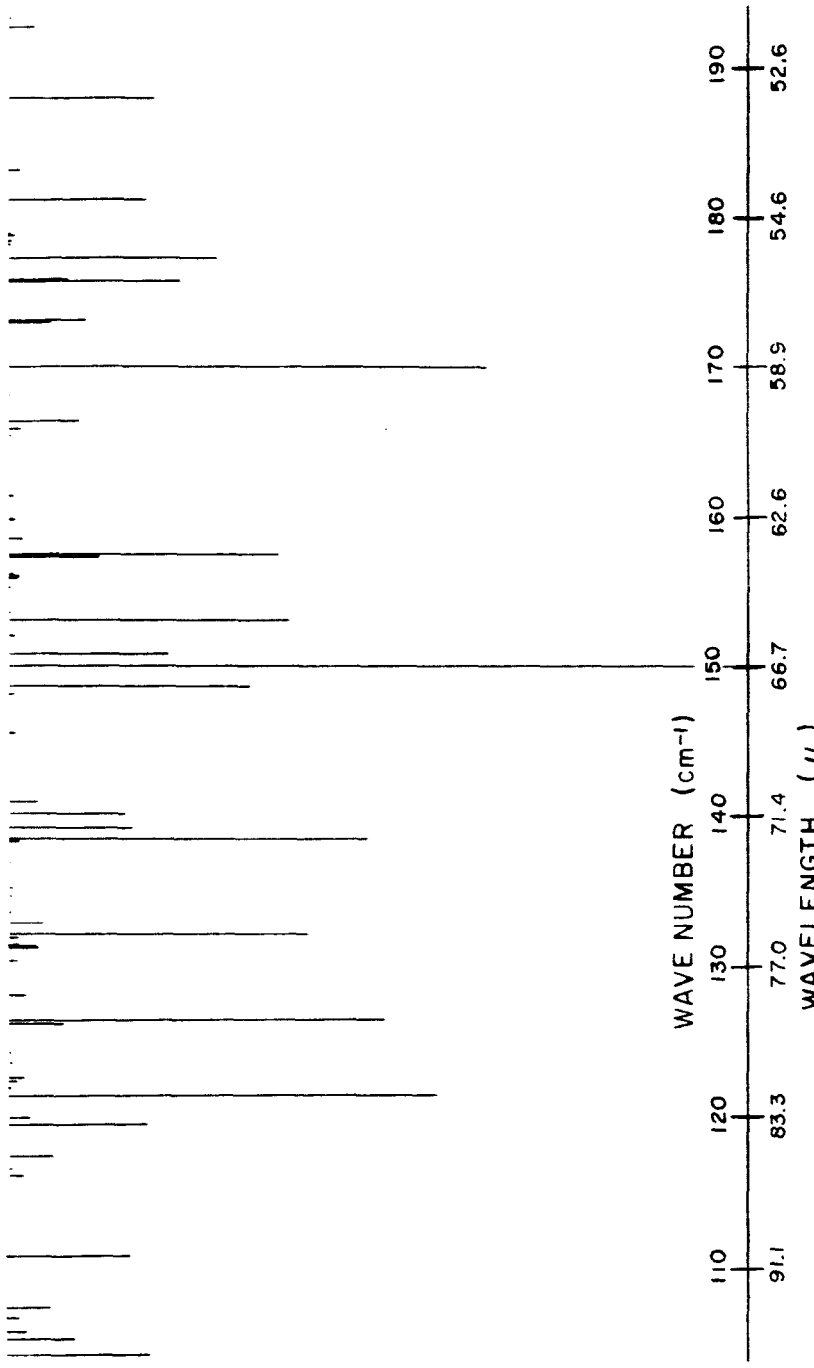

Fig. 4(cont.). A plot of Benedict's theoretical line positions and intensities from $\nu = 10\ cm^{-1}$ to $\nu = 200\ cm^{-1}$.

CHAPTER III
EXPERIMENTAL SETUP

A. System Outline

The equipment of this experiment consists of a 2500°K blackbody source, a 13 cps chopper with mechanical switches controlled by its shaft to generate a square reference signal, a 50-foot multi-traversal absorption cell, a Michelson type interferometer, a Texas Instrument Ge bolometer, a tunable amplifier, a correlator which multiplies the detector and the reference signals and integrates with respect to time, a dc amplifier, a chart recorder, and a digitizing unit which punches a paper tape according to the input voltage. Using an IBM 1620 computer the paper tape punches cards which an IBM 7094 computer uses to calculate the spectrum from the interferogram data. A block diagram of the setup is shown in Fig. 5.

The radiation emitted by the blackbody source is chopped at 13 cps and sent through the 50-foot multi-traversal absorption cell. The mirrors of the cell for the measurements reported were arranged to give a four traversal path, i.e., 200 feet equivalent pathlength (see Fig. 5). The outgoing beam from the absorption cell is then divided and recombined in the interferometer and detected with the Texas Instrument Model CTC germanium bolometer. The

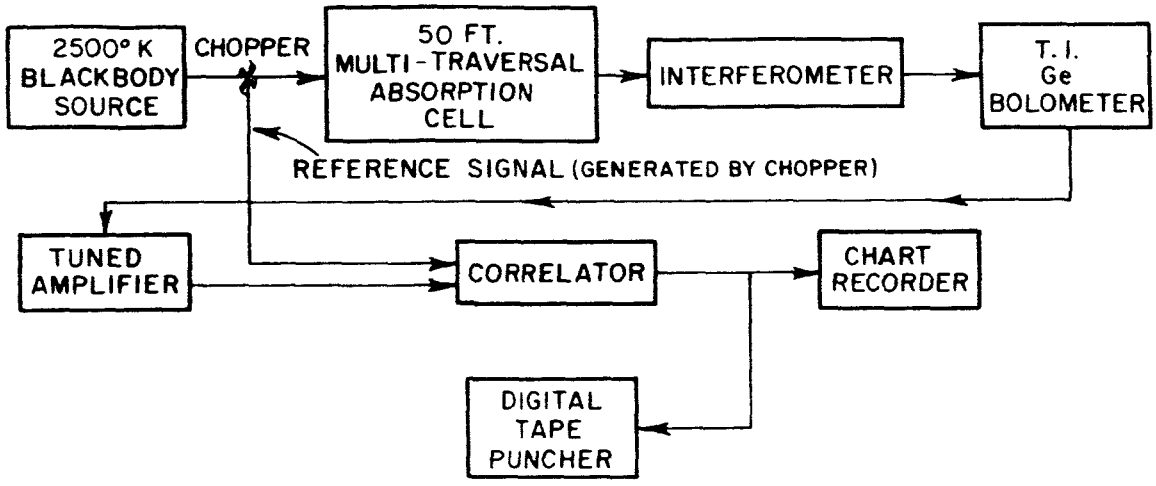

Fig. 5. A block diagram of the experimental setup.

output of the bolometer is amplified and then multiplied with the 13 cps square reference signal generated by the switches of the chopper. This product is integrated for a time which is long with respect to the period of the 13 cps signal to eliminate any unchopped optical noise and any electrical noise of frequencies other than 13 cps. The output of the correlator is apparently dc (when the movable mirror is not moving, of course). It is amplified with a dc amplifier and fed to both the chart recorder and the digitizing unit which punches the paper tapes required by the computers.

The blackbody is essentially an electrically heated carbon cone. The radiation is guided by a light pipe into the vacuum chamber. It is collimated by the $2\frac{1}{2}$" focal length, $2\frac{1}{2}$" diameter, spherical mirror and guided by the plane mirror into the absorption cell. The original optical design used a 45° plane mirror with a hole for the light pipe as shown in Fig. 6(a). However, calculations and practical measurements indicated that the aperture blockage of the plane mirror resulting from the insertion of the light pipe induces much more loss than the less collimated but larger aperture design shown in Fig. 6(b). Therefore, the latter setup is used.

The interferometer consists mainly of a 45° beam splitter to divide the incoming beam into halves. A fixed mirror and a movable mirror are placed 90° to each other so that their reflection recombines and interferes according to the position of the movable mirror. The recombined beam is then reflected by the 45° plane mirror in the detector vacuum chamber and collected by the 3-inch focal length, 4-inch diameter parabolic mirror. A design similar to that shown in Fig. 6(a) is used because here the mirror diameter is much larger than the light pipe diameter. The loss caused by that small portion of the aperture which is blocked is unimportant. The optical path to the interferometer and the bolometer is shown in Fig. 7. Figure 8 helps to visualize the relative positions of the source, the absorption cell, and the interferometer. A photograph is also presented in Fig. 9.

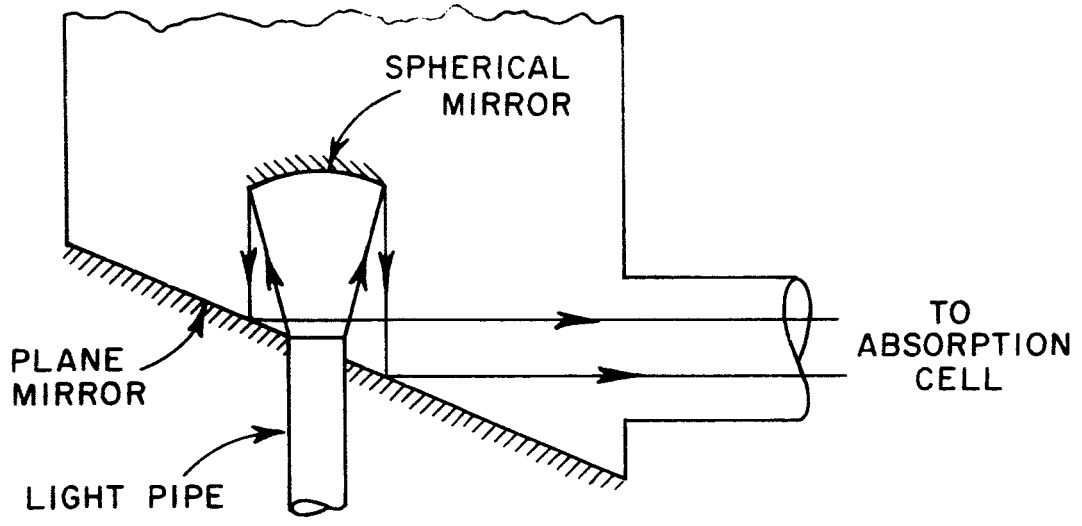

Fig. 6(a). The first optical design for the source.

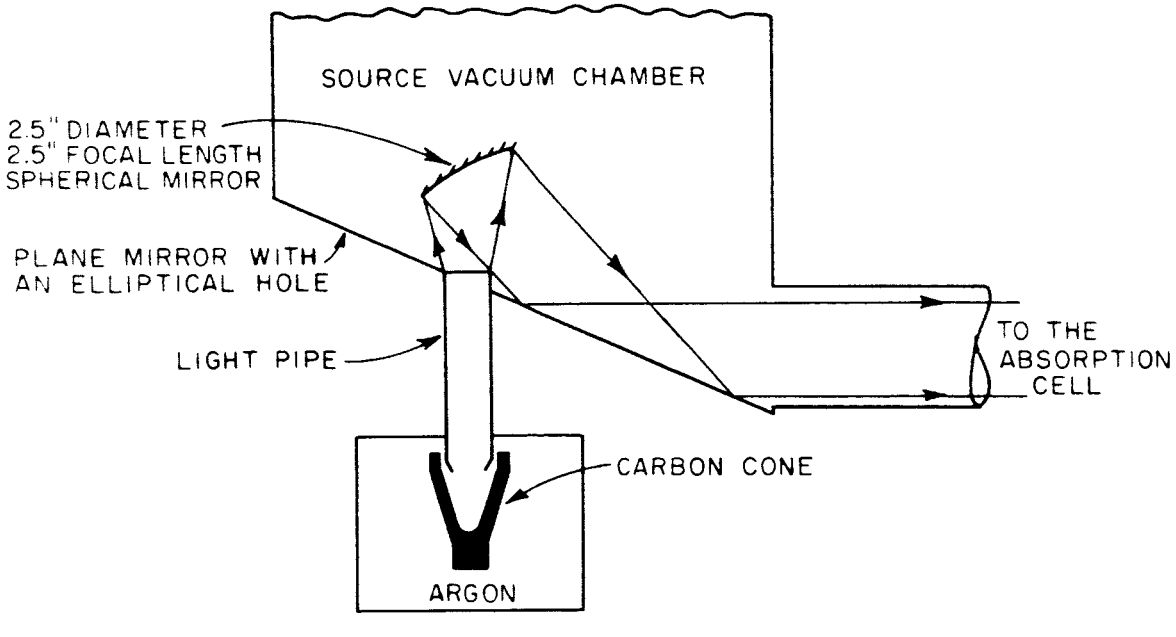

Fig. 6(b). The present optical design for the source.

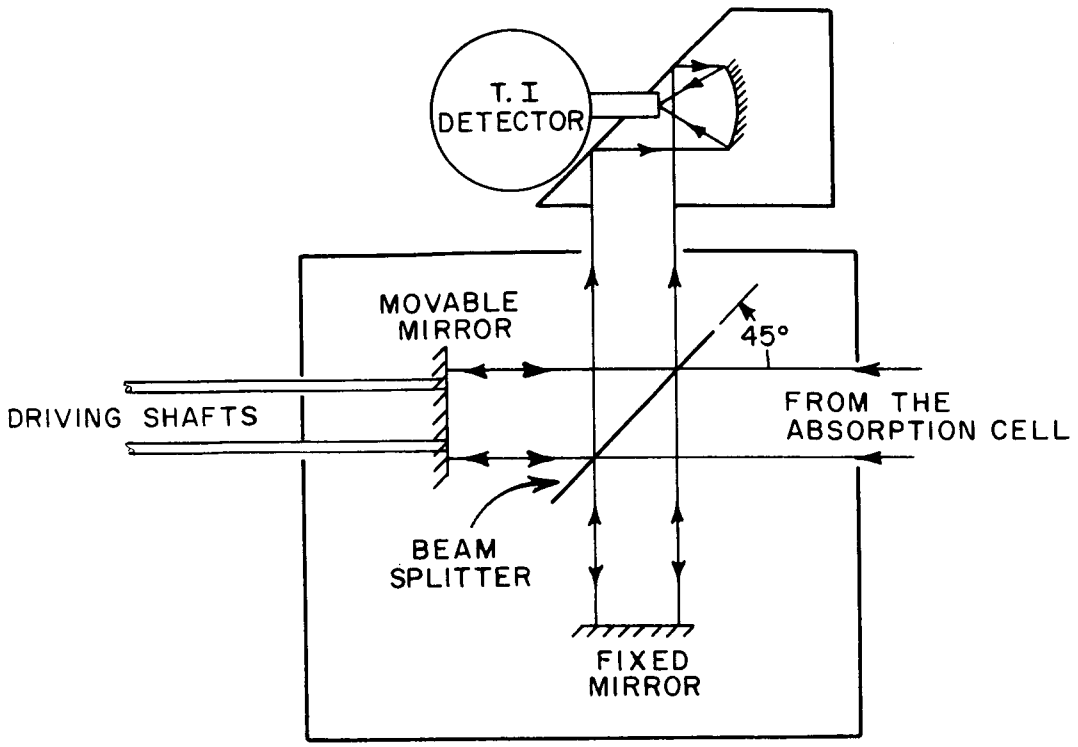

Fig. 7. The optical path to the interferometer and the detector.

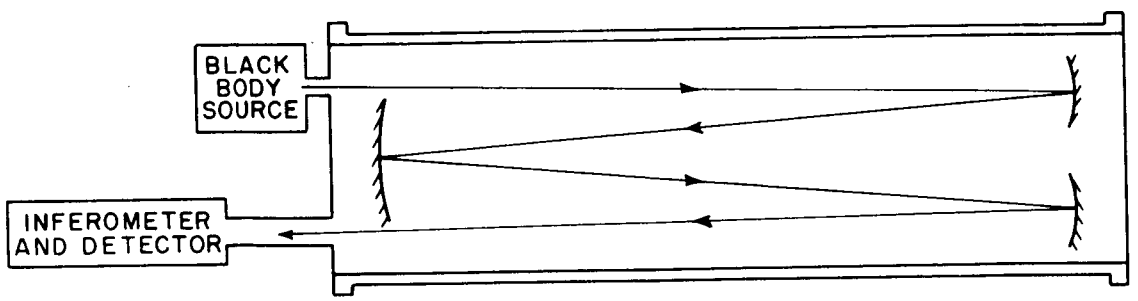

Fig. 8. Side view of the relative positions of the source, the absorption cell, and the interferometer.

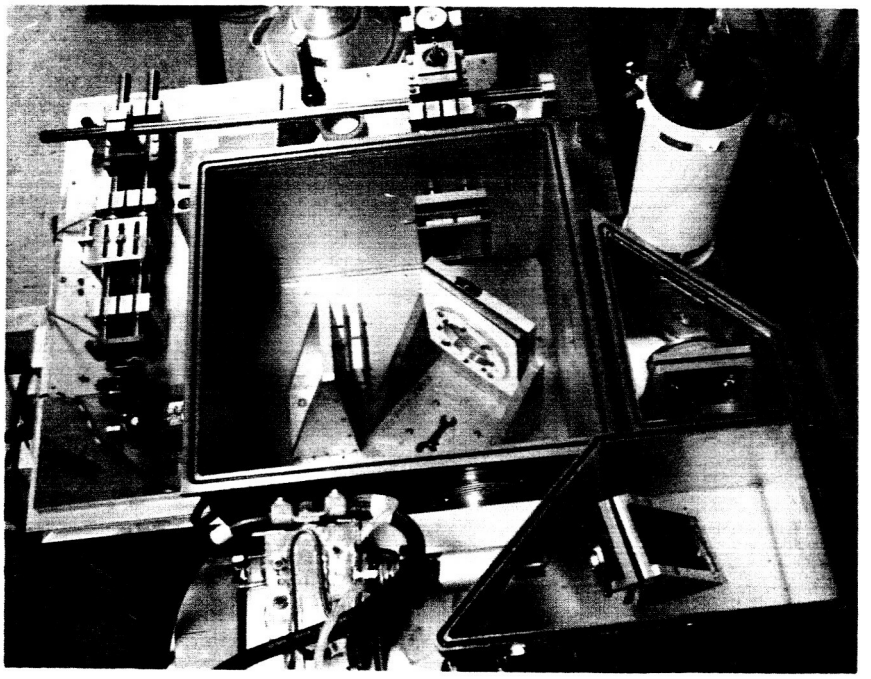

Fig. 9. A photograph of the source, the interferometer, and the detector.

Discussions on the blackbody source and the Michelson Interferometer will be given separately in the following two sections. For discussion on the absorption cell, see Reference 7. Reference 5 gives a discussion on the theory of the liquid-He-cooled Ge bolometer detector.

B. The Interferometer

The interferometer used was designed and previously used by Dr. R. A. Williams. A detailed discussion of it can be found in his dissertation. [18] This section discusses some aspects important to this experiment; namely, its principle, the resolution and bandwidth limitation, and the choice of a suitable beam splitter.

A top view schematic diagram of the interferometer is shown in Fig. 7. The most important parts of the interferometer are the wire-mesh beam splitter, the fixed front-surface plane mirror, and the movable front-surface plane mirror. Ideally one splits the incident radiation into halves so that one half illuminates the fixed mirror while the other half falls on the movable mirror. These signals are reflected and recombined. When the distance from the movable mirror to the beam splitter is $Y/2$ cm longer than the distance from the fixed mirror to the beam splitter, the detector receives the power spectral density

$$E_r(\nu, Y) = \frac{E_i(\nu)}{2} (1 + \cos 2\pi\nu Y) \quad \text{watt cm}, \tag{8}$$

where $E_i(\nu)$ is the power spectral density of the incoming radiation. Therefore, the total power that the detector receives is

$$I_r(Y) = \int_0^\infty E_r \, d\nu \tag{9}$$

or

$$(10) \qquad I_r(\gamma) = \frac{1}{2}\int_0^\infty E_i \, d\nu + \frac{1}{2}\int_0^\infty E_i \cos 2\pi \nu\gamma \, d\nu \text{ watt.}$$

This I_r can be measured to calculate E_i with the known values of I_r. Next the Fourier transform of I_r is performed, giving

$$(11) \qquad E_i(\nu) = 8\int_0^\infty I_r(\gamma)\cos 2\pi \nu\gamma \, d\gamma.$$

This is done with an IBM 7094 computer. Since γ has an upper limit, as will be discussed later, the numerical integration is only done up to γ_{max} instead of to infinity. The computed power spectral density $E_i'(\nu)$ is related to $E_i(\nu)$ in the following manner:

$$(12) \qquad E_i'(\nu) = \int_0^\infty E_i(\nu') \, \frac{\sin 2\pi\gamma_{max}(\nu-\nu')}{\pi(\nu-\nu')} \, d\nu' \, ;$$

i.e., $E_i'(\nu)$ is the convolution of the Fourier transform of $I_r(\gamma)$ and the Fourier transform of the function of γ of a low-pass filter which cuts off at $\gamma > \gamma_{max}$.

The working principle of the interferometer has been discussed. We notice that in order to get an absolutely correct spectrum it is necessary to have $\gamma_{max} = \infty$. This is impossible mechanically, but even before the mechanical limitation becomes a problem, γ_{max} is further limited by insufficient signal-to-noise ratio, and the length of experiment time.

Having $\gamma = \gamma_{max}$ imposes a limit on the bandwidth and resolution of the instrument. To see this, it is important to notice that the experimental total power curve obtained is $I_r'(\gamma) = I_r(\gamma)\, W(\gamma)$, where $W(\gamma) = 1$ in the range $-\gamma_{max} \leq \gamma \leq \gamma_{max}$ and is zero elsewhere.

Using the convolution theorem, one gets

$$E_r'(\nu) = F^{-1}[I_r^{-1}(\gamma)] = \int_0^\infty E_i(\nu') \frac{\sin 2\pi\gamma_{max}(\nu-\nu')}{\pi(\nu'-\nu')}\, d\nu' . \tag{12}$$

The function $\frac{\sin 2\pi\gamma_{max}\nu}{\pi\nu}$ has a well-known bandwidth of $\frac{1}{\gamma_{max}}$; i.e., any lines within $\frac{1}{\gamma_{max}}$ cannot be resolved. In other words, the resolution is $\frac{1}{\gamma_{max}}$. Therefore, it is obvious that one thinks of increasing γ_{max} for best resolution. The first difficulty to obtain larger γ_{max} lies in the fact that an interference pattern has a large peak at $\gamma = 0$ while the consecutive peaks decrease as γ increases. Noise level is constant through the γ spectrum. Therefore, when the magnitude of the peak becomes close to the magnitude of noise, increasing γ further is fruitless. The second difficulty results from the impossibility of increasing experiment time indefinitely. Since the integration circuit has a definite response time, the movable mirror has a definite speed limit. This means for larger γ_{max} longer running time has to be used. But the source output, detector

response, and the dc bias of the electronics are all functions of long time. Experiment time cannot be increased at will.

It is found that a satisfactory signal-to-noise ratio and reasonable running time are obtained with a Y_{max} of 7800μ microns; however, because of the total evaporation of liquid He in the detector at 5400μ in one of the water vapor runs, some experimental results are given with a Y_{max} of 5400μ.

Besides the $Y \leq Y_{max}$ limitation, since glass is opaque in the submillimeter region, conventional $\frac{1}{2}$ transmission silver-deposited glass does not work for a beam splitter; wire meshes are used instead. Meshes of different wire density work in different ranges. From Williams [18] experimental results, it is observed that a 200-lines-per-inch mesh works best from 140μ to 350μ; a 500 LPI mesh works best from 80μ to 110μ. The region covered by the 200 LPI mesh is less explored, so the initial experiment was done with the 200 LPI mesh beam splitter.

C. The Blackbody Source

There are very few types of sources available in the submillimeter region. Thermal radiation is the most common means used to generate submillimeter energy. The idea of using a high-temperature carbon furnace as an infrared source was investigated by R. L. Spanbauer. [19]

He applied 200 amps from a 6 volt power supply to a $\frac{1}{2}$-inch diameter, 2-inch long, carbon rod which then became a very intense source for his slit spectrometer. But, since a circular source is necessary for a Michelson interferometer, a cone-shaped carbon element was used instead of a rod. Except for the changes necessary for a cone-shaped carbon, most of the design follows his experience. The mechanical structure was designed by D. B. Rensch and R. A. Williams. It was then tested and modified by the author to make it operative at higher temperatures. C. H. Boehnker designed a cone for uniform brightness.

As mentioned, our source is essentially a carbon cone heated by a strong current; 6 Kw is consumed in a 0.4 cubic inch carbon cone. Because of this high power density, the electrodes and the container must be water cooled. To prevent combustion and evaporation of the carbon, the entire box is constantly flushed with argon at a pressure of 3 to 10 lb per square inch higher than atmospheric pressure. To guide the radiation from the core of the cone to the optics in the source vacuum chamber, a light pipe is used. A schematic drawing and a photograph of the source is shown in Fig. 10 and Fig. 11, respectively.

The dimensions of the carbon cone are shown in Fig. 12. To obtain higher temperature with weaker current, the cone must be as thin as possible. The 1/16-inch thickness is almost the thinnest

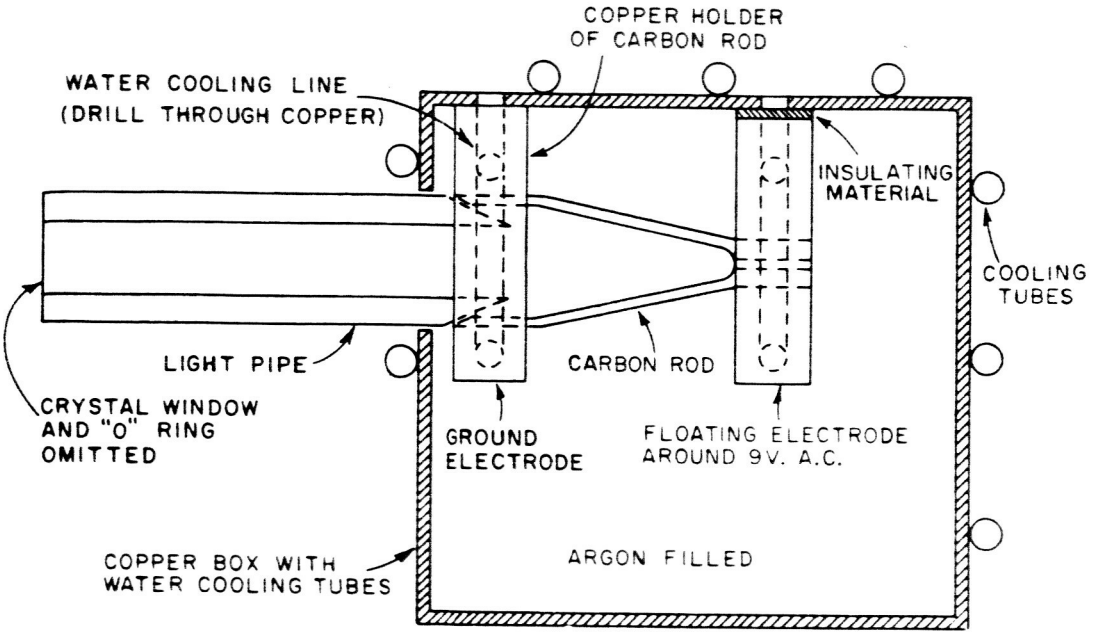

Fig. 10. A schematic drawing of the source.

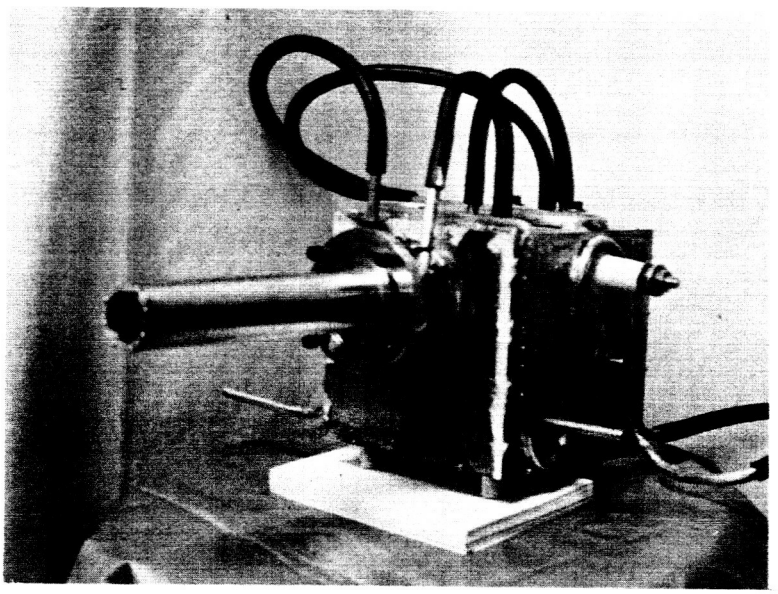

Fig. 11. A photograph of the source.

that is machinable. Moreover, to achieve uniform brightness the cone should be thinner at the larger part and thicker at the smaller part. A theoretical curve was calculated, then linearlized for machining.

A schematic drawing of the cone-holding electrodes is shown in Fig. 13. It is seen that a two-piece design would give a better surface contact. In fact, this was attempted but abandoned because of the tedious task of preventing water leaks every time the electrodes are disassembled for cone replacement. The present design is free of water leaks. To assure a better surface contact, the cone-contacting surfaces are coated with a fine graphite powder before attaching them to the electrodes.

A 20KVA multi-step welding transformer is used to supply low-voltage, strong current to the source and an optical pyrometer is used to measure the cone temperature. Values of cone voltage and amperage were taken under different operating temperatures and are given in Table IV. The power fed to the cone and the cone resistance-versus-temperature are plotted in Fig. 14.

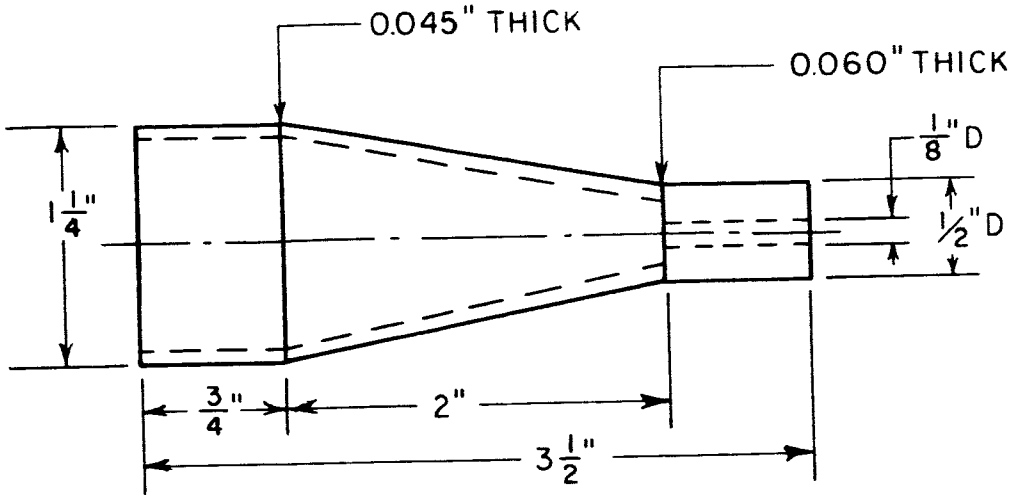

Fig. 12. Exact dimensions of the carbon cone.

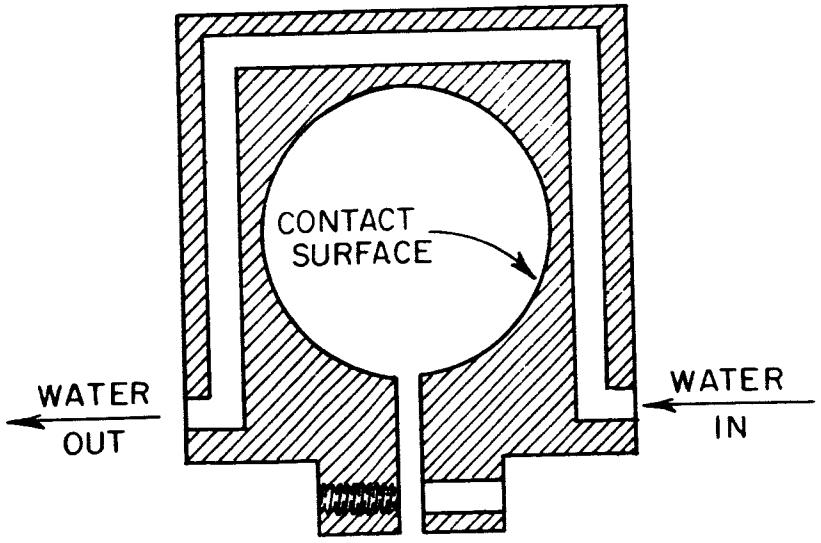

Fig. 13. A schematic drawing of the cone-holding electrode.

TABLE IV

Data on the Volt-amp. Characteristics of the Carbon Cone at Different Temperatures

Temperature (°C)	Voltage (volt)	Current (amp)	Power (watt)	Resistance (mΩ)
940	4.0	152	608	25.3
1220	5.0	220	1100	22.7
1445	6.0	280	1680	21.4
1675	7.0	360	2520	19.5
1785	7.5	410	3080	18.3
2115	9.0	600	5400	15.0
2300	9.0	680	6120	13.2

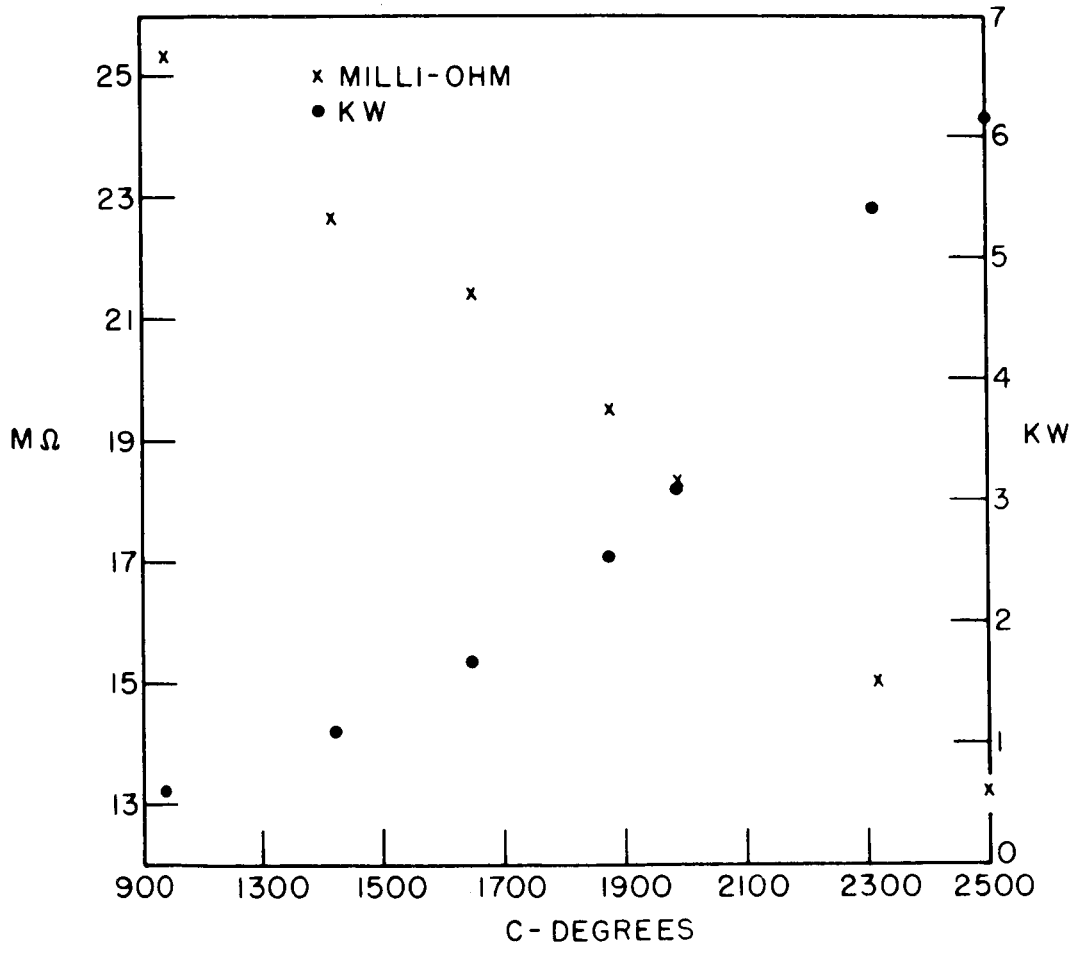

Fig. 14. Cone resistance and the power dissipated versus temperature.

The spectral power distribution and output power of the source is estimated by comparison with a perfect blackbody. The radiation from a perfect blackbody peaks up at T = 2.9°K for λ_{peak} = 1000μ and T = 289°K for λ_{peak} = 10μ, which are highly impractical to use since the intensity of the output is low. The scheme is, therefore, to increase the temperature in spite of the peaking up at higher frequencies. To obtain more signal, it is necessary only to increase the temperature of the source. Of course, the temperature can not be higher than the melting point of carbon. In fact, problems arise even before the carbon melts. As seen in Table IV, the highest temperature achieved was 2300°C. Further increase of temperature would introduce problems such as insufficient cooling capacity, overheated leads, loose electrode-to-cone contact caused by the larger heat expansion coefficient of copper to that of carbon, and the short life of the carbon.

In the future a new model of this source will be built incorporating several improvements. There is no way to solve the cooling problem which prevented our source from being used above 2300°C except to build a new source with higher cooling capacity and larger conducting elements. The Ni36 alloy is proposed to be used as electrode material instead of copper because of its low

thermal expansion. Carbon materials such as National "AVC" and "ATJ" which are purer and more machinable will be tried for less noisy output, higher achievable temperature, longer life, and lower operating current. Higher argon pressure will be used to prevent evaporation after a stronger box is built.

The source being used is capable of giving useful signal and a reasonable lifetime at 5.6 volts and 200 amps (i.e., approximately 1200°C) for a pathlength of 200 ft and a water vapor pressure of 6 mm Hg or less. It will be used until an increase of the signal intensity is necessary.

CHAPTER IV
EXPERIMENTAL RESULTS

To demonstrate the use of the equipment described in the preceding chapters, two experiments have been conducted, each consisting of two tests. First, a vacuum test at a pressure of 0.009μ Hg is run and then a water vapor test is conducted. In the first experiment, the water vapor pressure was 4.42 mm Hg. A path-length of 200 ft was used, giving 0.0265 precipitable centimeters of H_2O. The second experiment consisted of a vacuum run at a pressure of 0.02μ Hg and a water vapor test at a pressure of 1.1 mm Hg or 0.00663 pr-cm. In the first experiment, the liquid helium which cools the detector ran out at $\frac{\gamma_m}{2} = 5400\mu$ as mentioned in Chapter III, section B. The pressure of 4.42 mm Hg in the first experiment was chosen to give an absorption intensity close to that of the water vapor in normal atmosphere. However, neutral broadening gas was not used in these initial tests. In the second experiment, both tests were completed up to $\frac{\gamma_m}{2} = 7800\mu$ and the gain setting of the pre-amplifier of the detector was kept constant to enable accurate comparison between the vacuum test and the water vapor test. The water vapor pressure was decreased in order to reduce broadening effects and permit observation of more closely spaced lines. The conditions of the four tests are summarized in the following table:

Test	gas	pressure	$\frac{\gamma_m}{2}$	preamp gain
1	atmosphere	0.009μ	7800μ	at the calibration mark
2	water	4.4 mm	5400μ	at the 2.5 mark
3	atmosphere	0.02μ	7800μ	at the 3.7 mark
4	water	1.1 mm	7800μ	at the 3.7 mark

All tests were conducted with 5.6 volts, 200 amperes on the source and a pathlength of 200 feet.

As the movable mirror is scanning, an analog-to-digital digitizing unit punches tape according to the output of the amplifiers, i.e., the interferogram. The tape is then fed into an IBM 1620 computer to punch computer cards for the Fourier transform program for the IBM 7094 computer. The interferogram of test 1 recorded by the digitizing unit is shown in Fig. 15.

To make the Fourier transform of the constant term in Eq. (10) vanish, integration must be accomplished with $d\nu = n/\gamma_m$. Since test 2 was stopped at $\gamma_m/2 = 5400\mu$, $d\nu$ was chosen to $0.46296296\ cm^{-1}$. Test 1 could be integrated with a smaller $d\nu$, but in order to compare test 2 with test 1, test 1 was also integrated with $d\nu = 0.46296296\ cm^{-1}$. Test 3 and test 4 were both completed at $\gamma_m/2 = 7800\mu$, so they were integrated with $d\nu = 0.32051382\ cm^{-1}$. We readily see that the resolution for test 1 and 2 is $0.46296296\ cm^{-1}$, while the resolution for tests 3 and 4 is $0.32051382\ cm^{-1}$.

The Fourier transforms of the interferogram of the four tests are shown in Figs. 16, 17, 18, and 19. Imposed on Figs. 17 and 19 are the calculated line positions and intensity from Benedict, as shown in Fig. 4. Within the region 140 to 350μ the experimental lines agree with most of the theoretical lines in both tests 2 and 4. Each of the line groups (36.59 cm^{-1}, 37.13 cm^{-1}), (55.29 cm^{-1}, 55.43 cm^{-1}, and 55.69 cm^{-1}), and (58.89 cm^{-1}, 59.70 cm^{-1}, and 59.95 cm^{-1}) appears as a broad line in test 2 but they are resolved in test 4. Also, each line in test 2 is more intense and broader than that in test 4. This is a necessary result of the increase of absorption caused by increased pressure and the pressure-broadening effects.

Figure 20 is the imposition of test 1 evaluated for $\gamma_m/2$ = 3900μ and the same test evaluated for $\gamma_m/2$ = 7800μ. Larger γ_m gives better resolution, as seen in the figure and as explained by the theory in Chapter III.

Line positions can be read from the computer print-out with an accuracy of 0.04% of the wavenumber of the line according to the limit of the instrument, but they are not published here for two reasons: First, further calibration using gases with line positions which are well known (namely, N_2O, HCN, or CO) is desirable to check the calibration of the instrument; and secondly, the constant

term in Eq. (10) can be removed by subtracting it from the interferogram with the result that $d\nu$ can then be greatly decreased and the position of a line can be located much more accurately. Since decreasing $d\nu$ increases expensive computer time, line position studies will be done only on the best results of the later work.

To compare the water-vapor test with the vacuum test, one more computer program is done to evaluate the ratio of the value of the Fourier transform output of the water-vapor test to that of the vacuum test; to compute the natural logarithm of the ratio (which gives the attenuation constant α); and to evaluate the logarithm of the ratio (which gives the db attenuation). The results in the region 25.4 cm^{-1} to 105 cm^{-1} are shown in Figs. 21, 22, and 23. The line positions again check with the calculated positions, but the line intensities do not agree with Benedict's values. The disagreement might be caused by the non-uniform beam-splitter efficiency. A gas with known transition intensity should be tested for calibration of this effect. On the other hand, an ideal absorption spectrum should give no negative values but negative values are observed in the Fourier transform output of the tests. The presence of these numbers in the division computation is very undesirable. It may also cause the intensity disagreement.

After the above problem is solved, several tests at reduced pressures and longer pathlengths will be performed to obtain well-resolved lines. The attenuation coefficient-versus-pathlength will also be investigated. Then the nitrogen-broadening effect can easily be examined by filling the absorption cell with definite amounts of water-vapor and nitrogen evaporated from liquid nitrogen.

The four tests which were conducted have satisfactorily shown the possibility of using the system for more detailed investigation. Gases other than water-vapor should also be investigated in this very rarely explored submillimeter region.

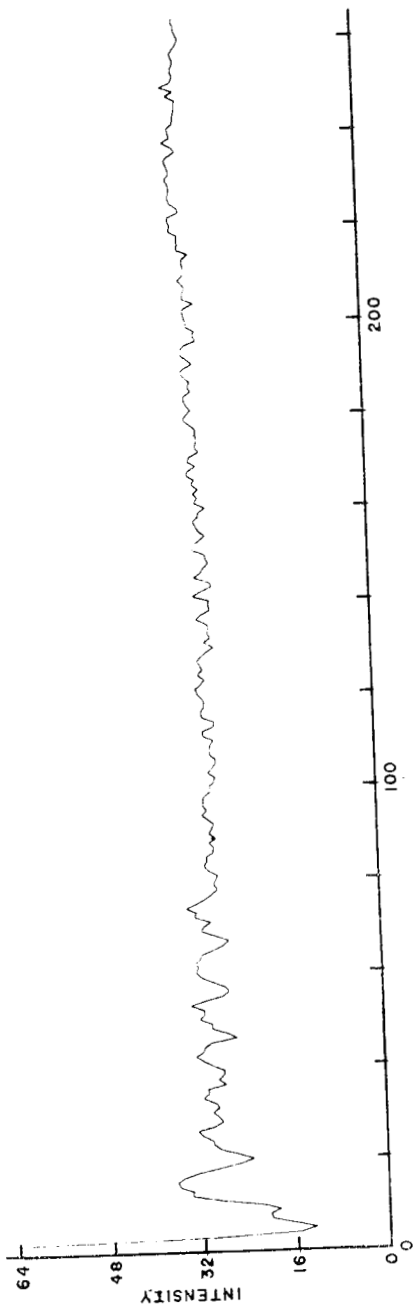

Fig. 15. The interferogram of test one.

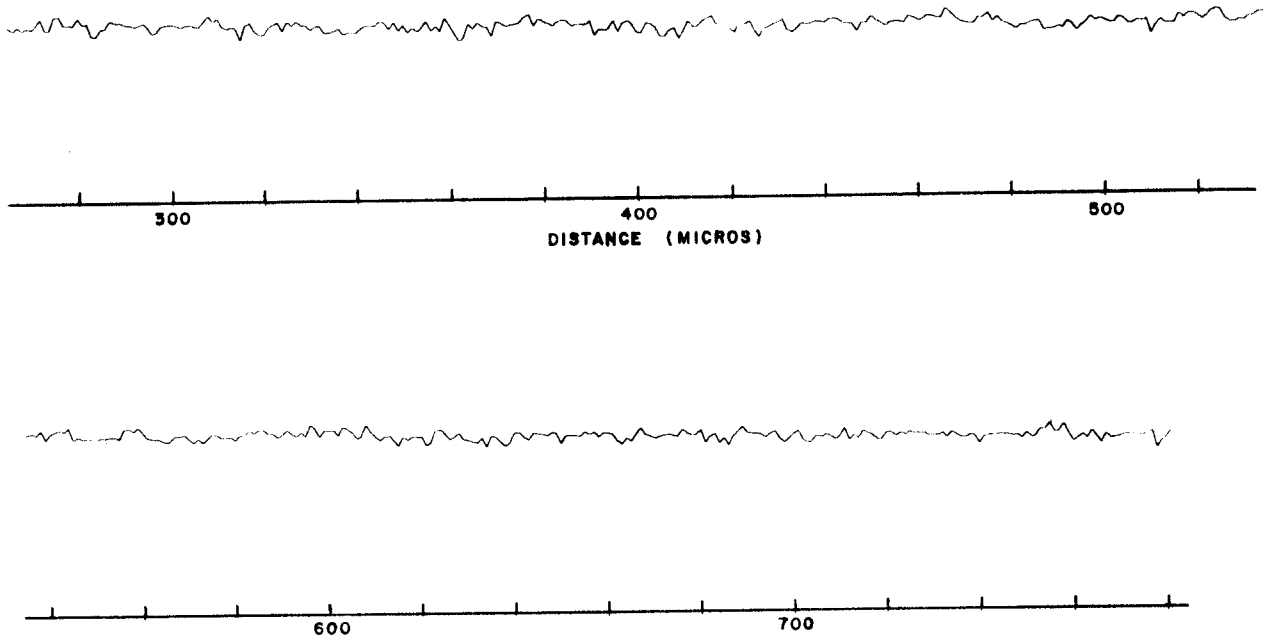

Fig. 15(cont.). The interferogram of test one.

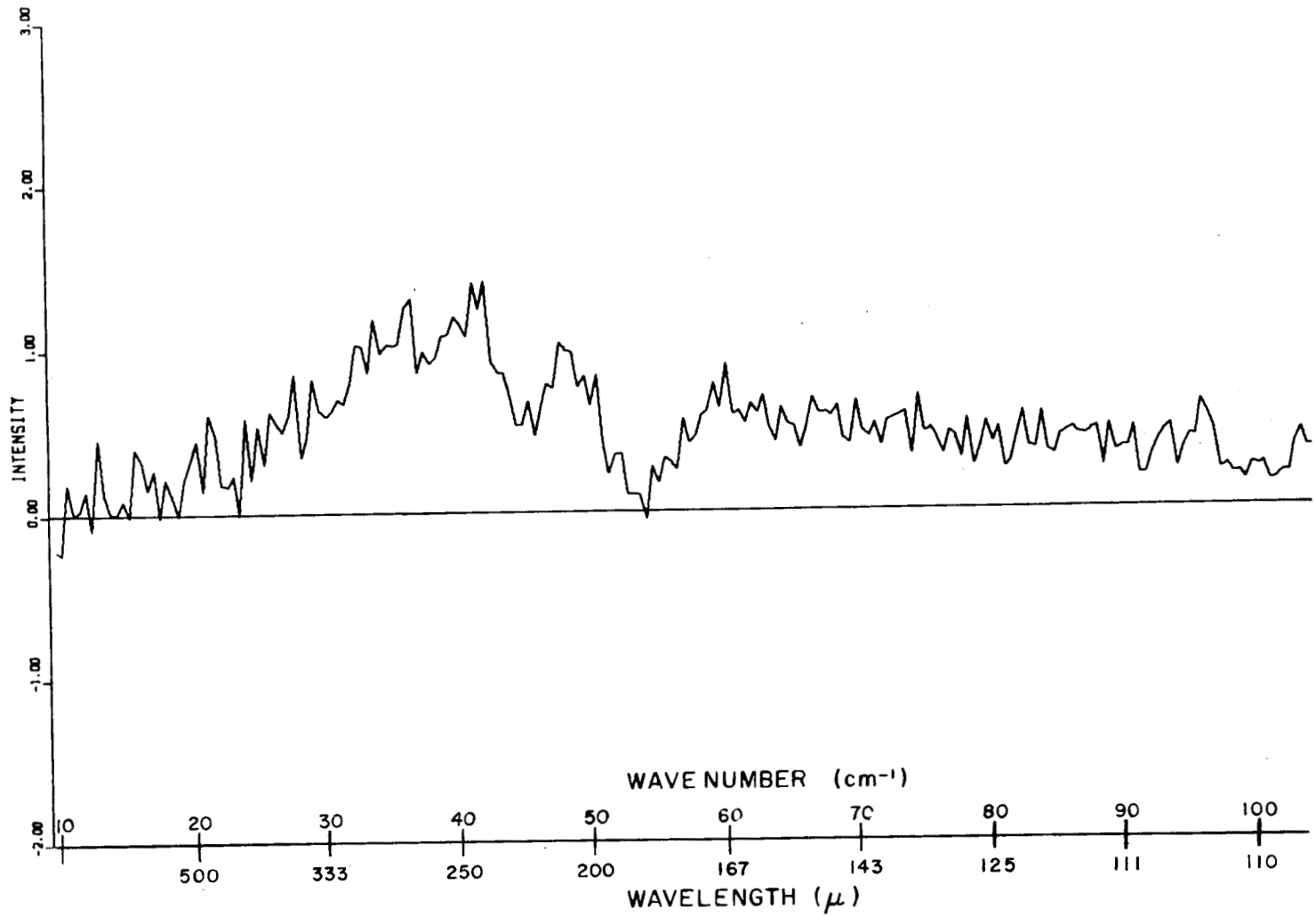

Fig. 16. The frequency spectrum from test one.

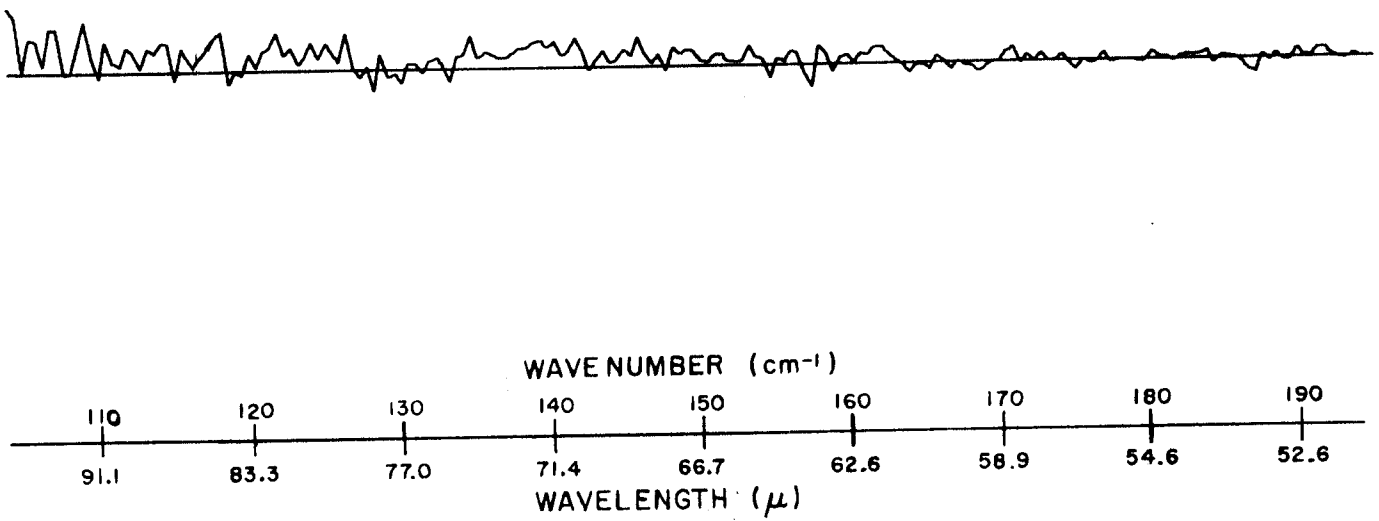

Fig. 16(cont.). The frequency spectrum from test one.

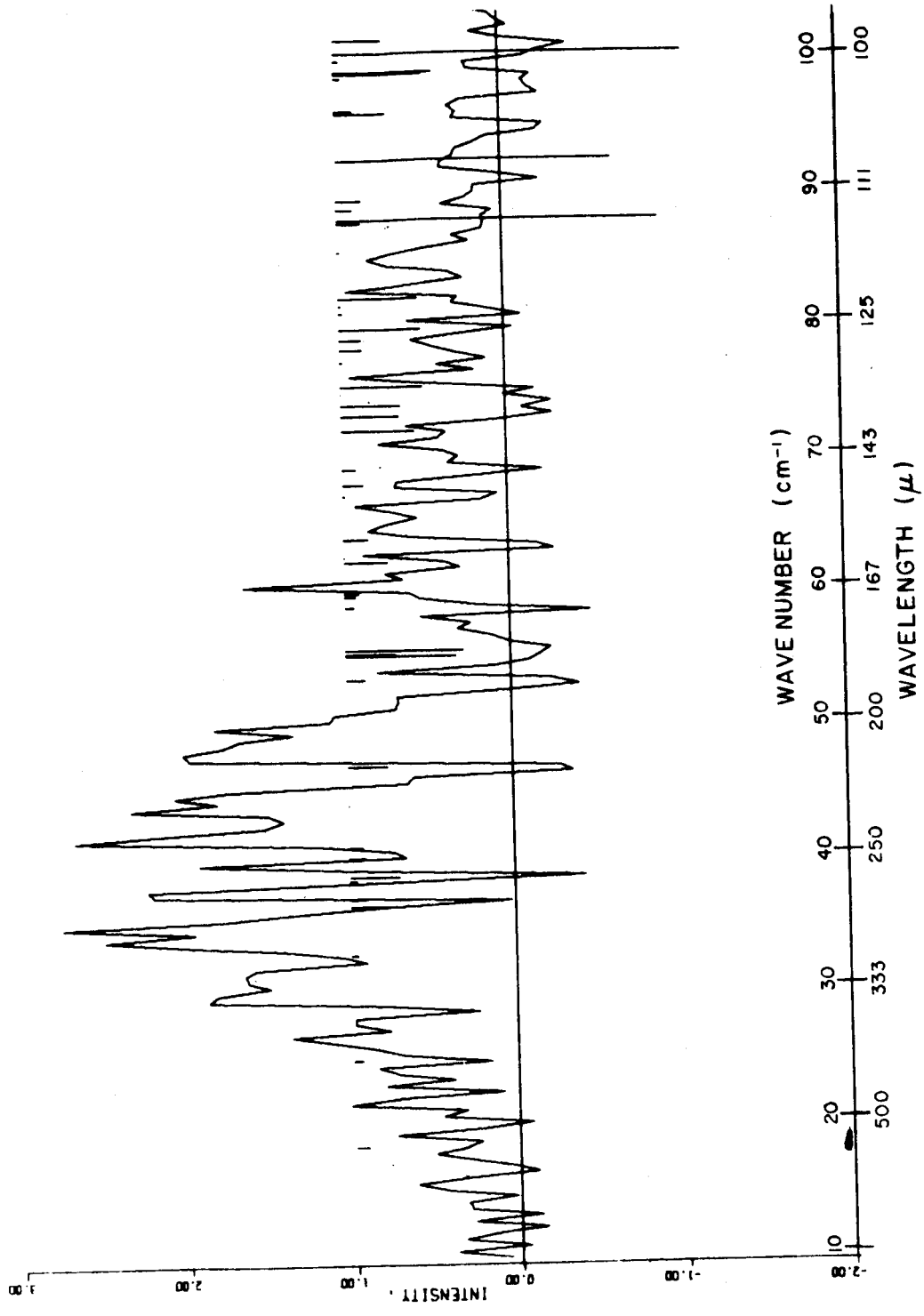

Fig. 17. The frequency spectrum from test two.

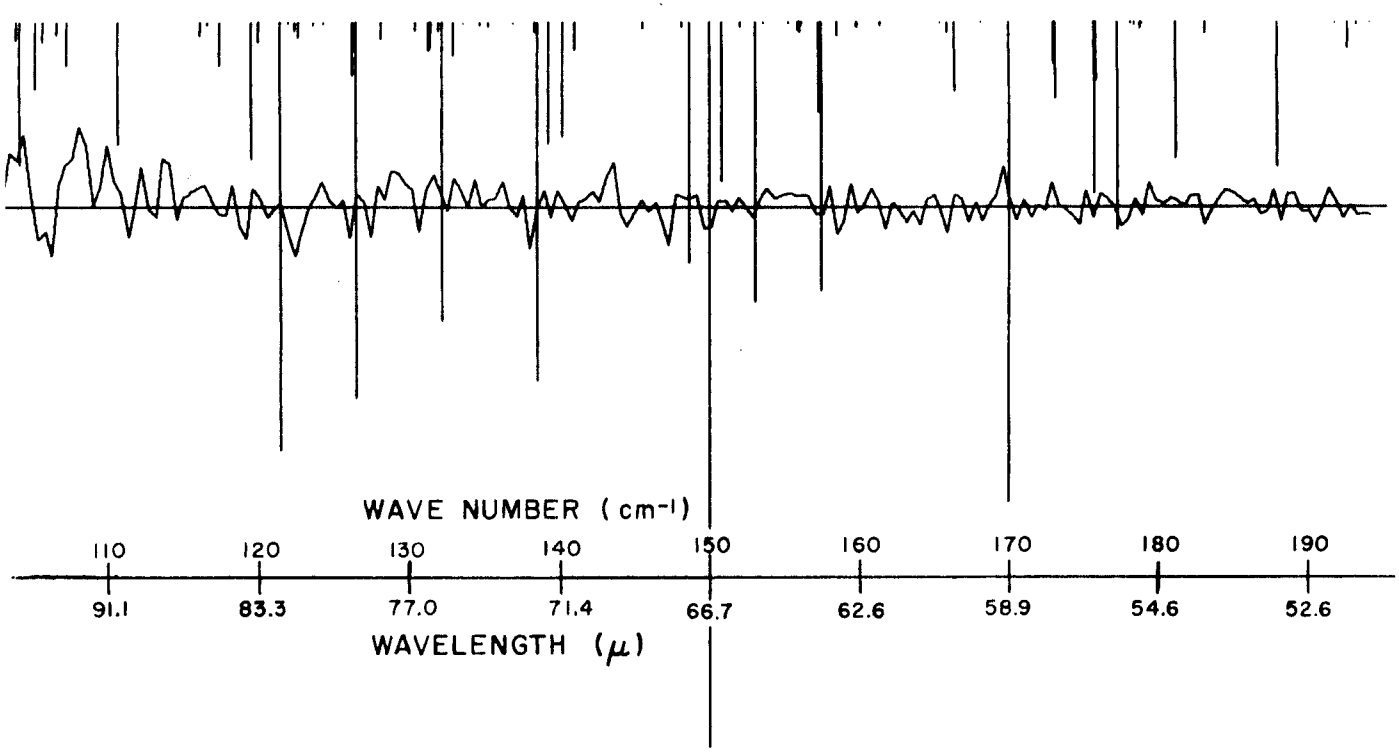

Fig. 17(cont.). The frequency spectrum from test two.

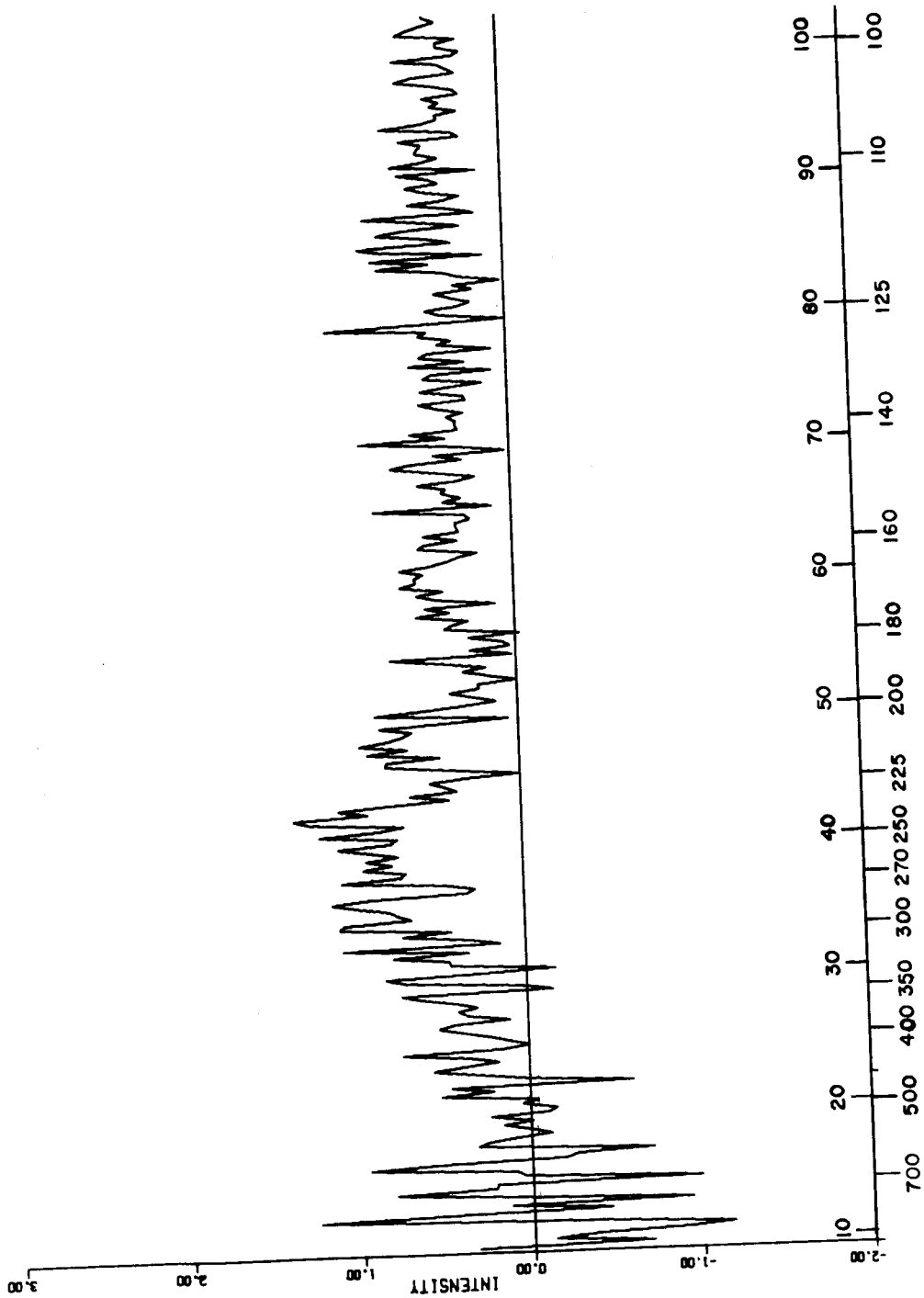

Fig. 18. The frequency spectrum from test three.

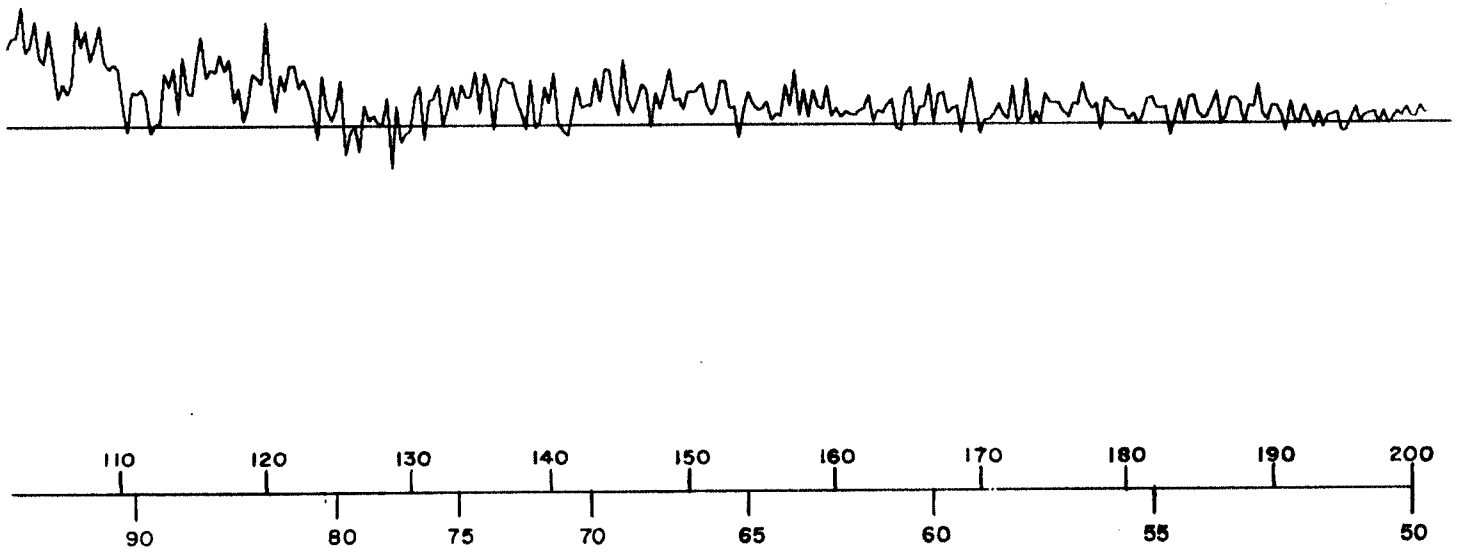

Fig. 18(cont.). The frequency spectrum from test three.

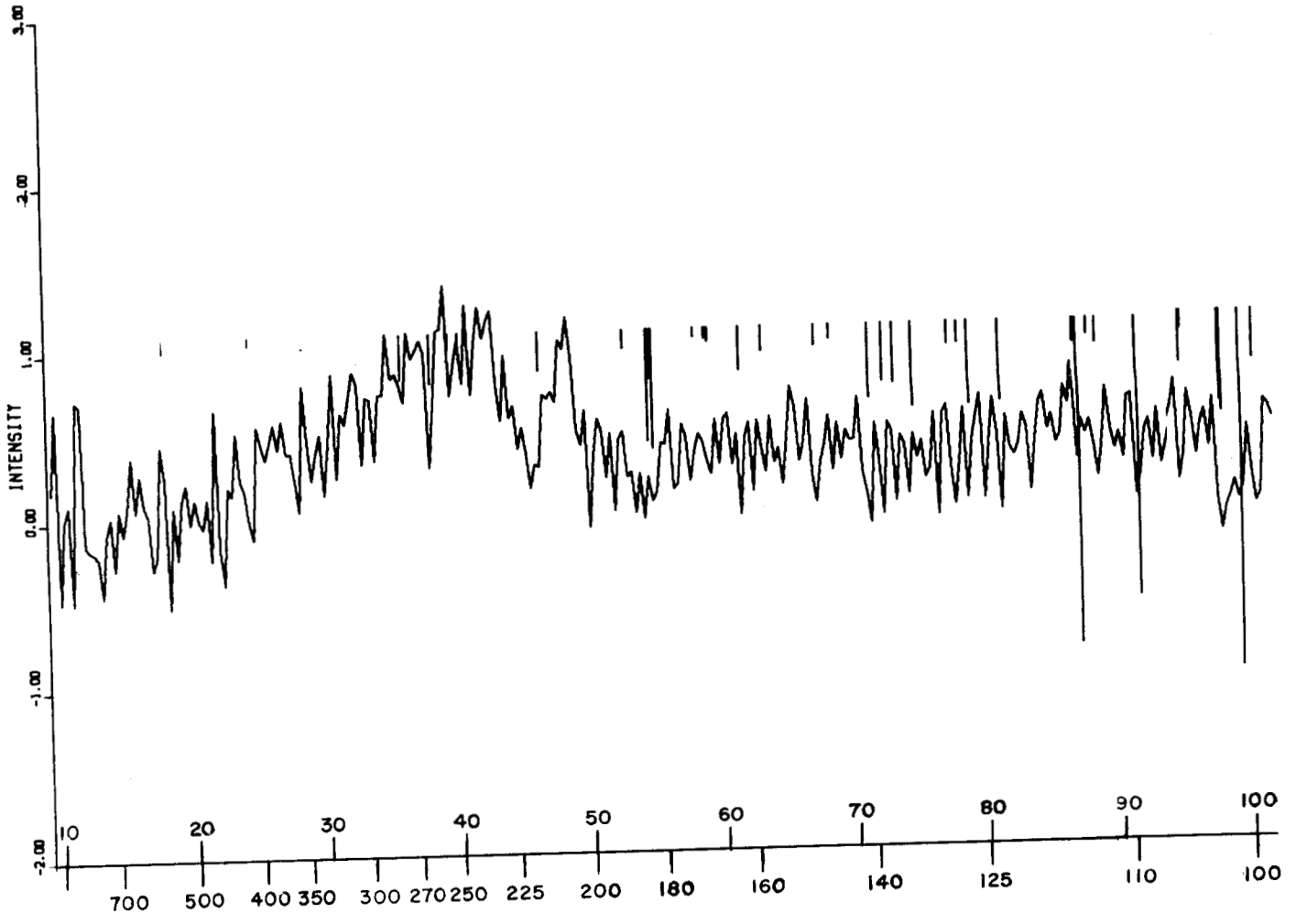

Fig. 19. The frequency spectrum from test four.

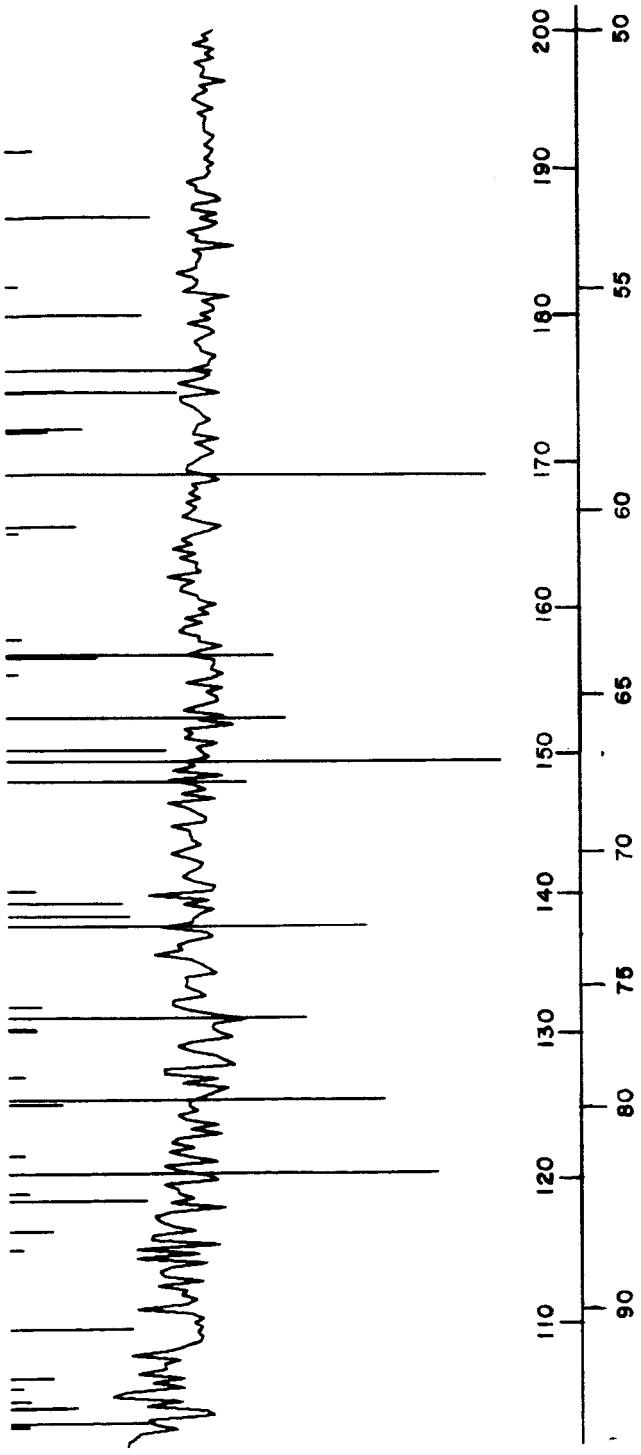

Fig. 19(cont.). The frequency spectrum from test four.

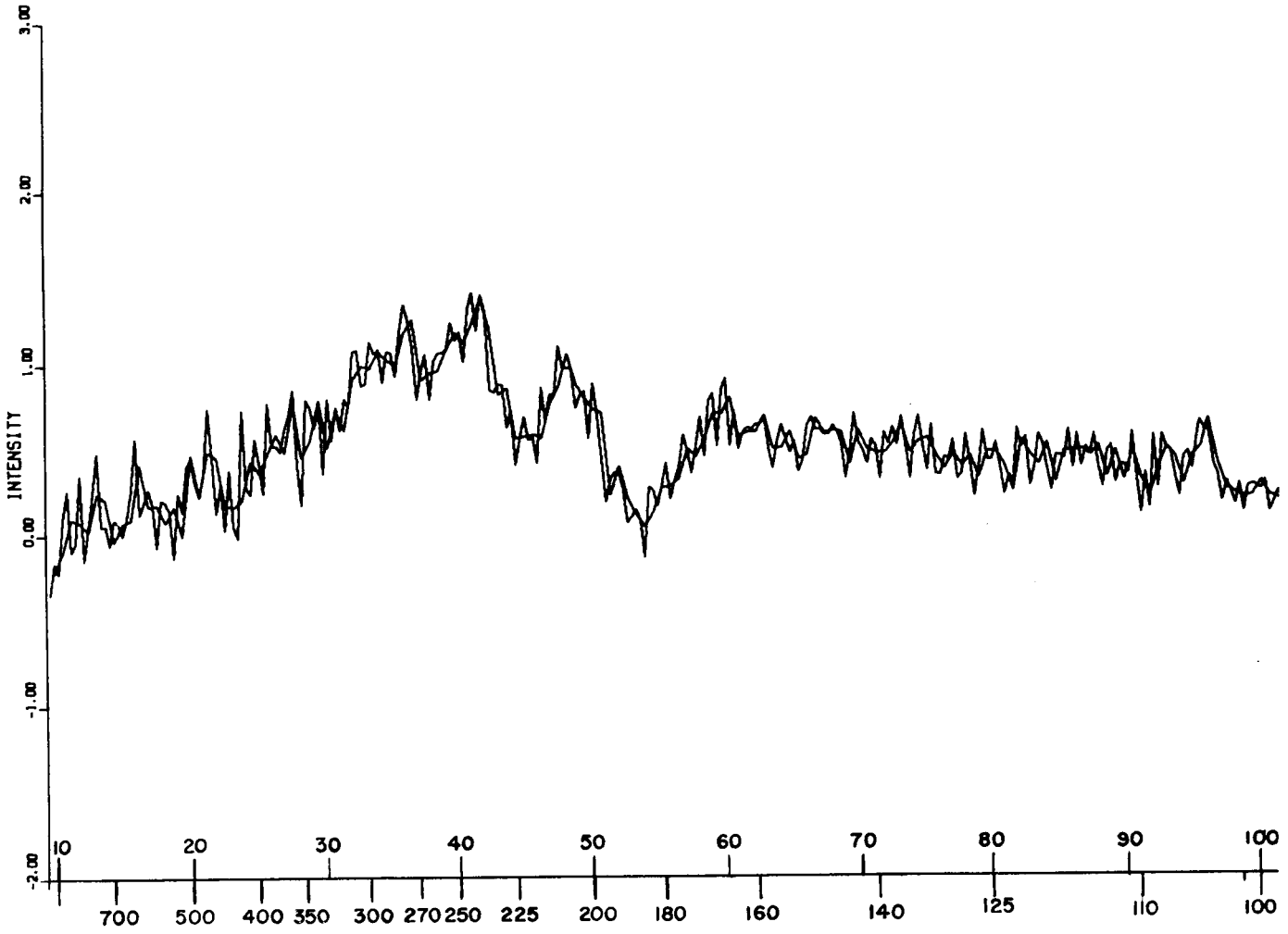

Fig. 20. A comparison of the frequency spectra of test one evaluated with a different γ_m.

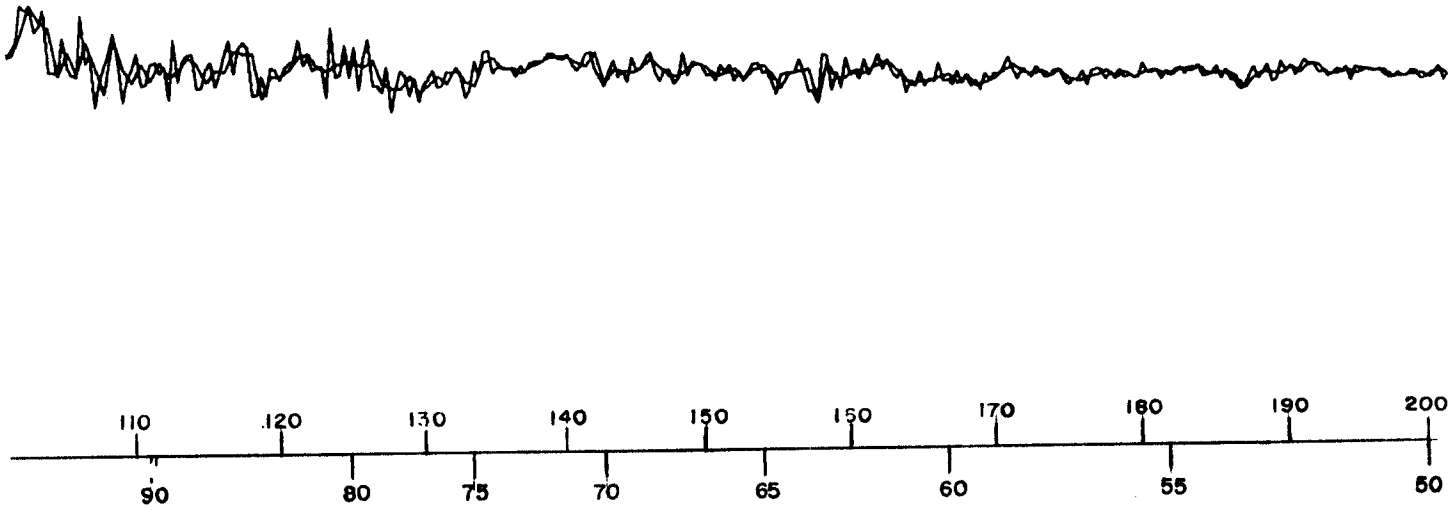

Fig. 20(cont.). A comparison of the frequency spectra of test one evaluated with a different γ_m.

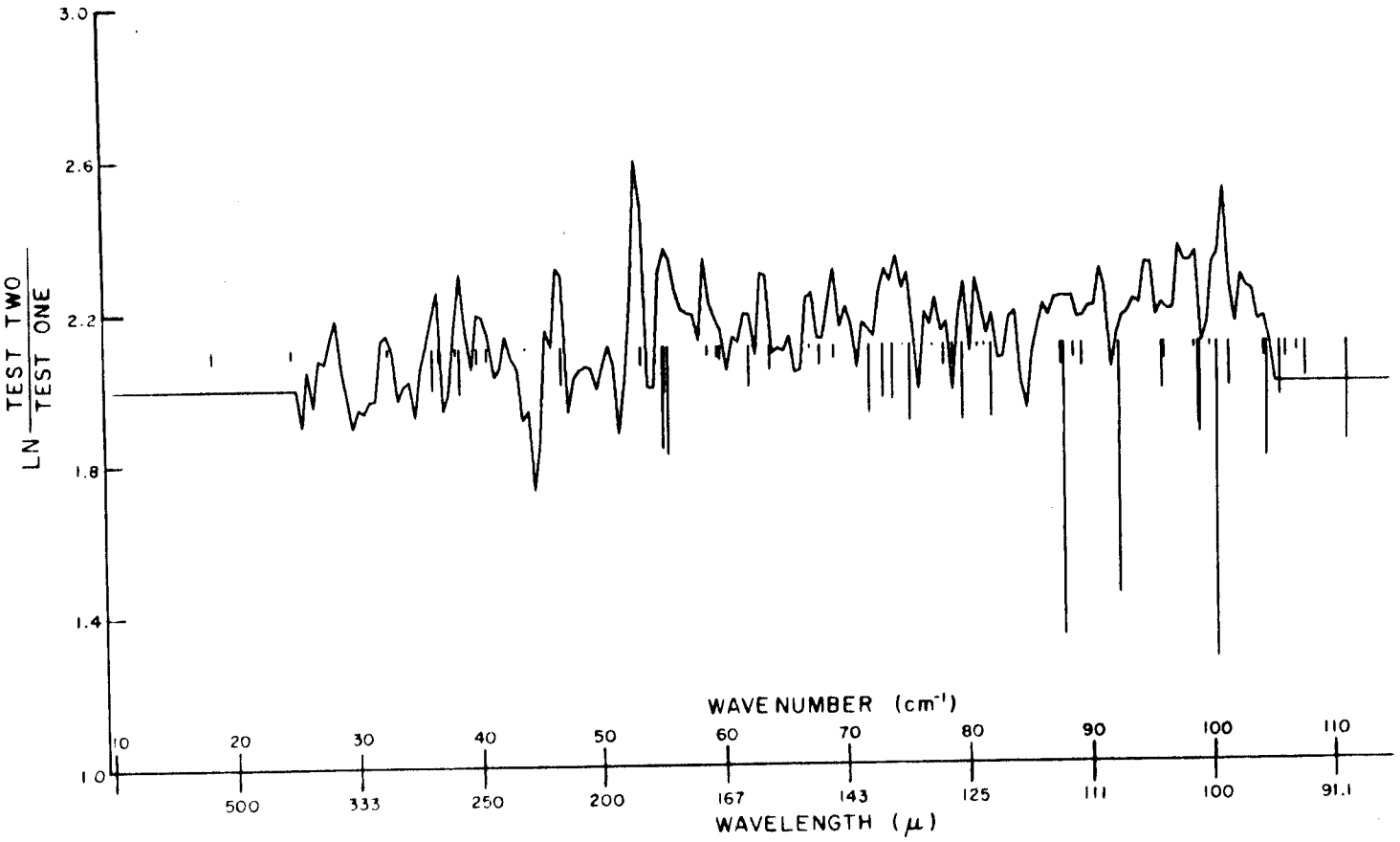

Fig. 22. The plot of the natural logarithm of Fig. 21. Absorption is plotted upwards.

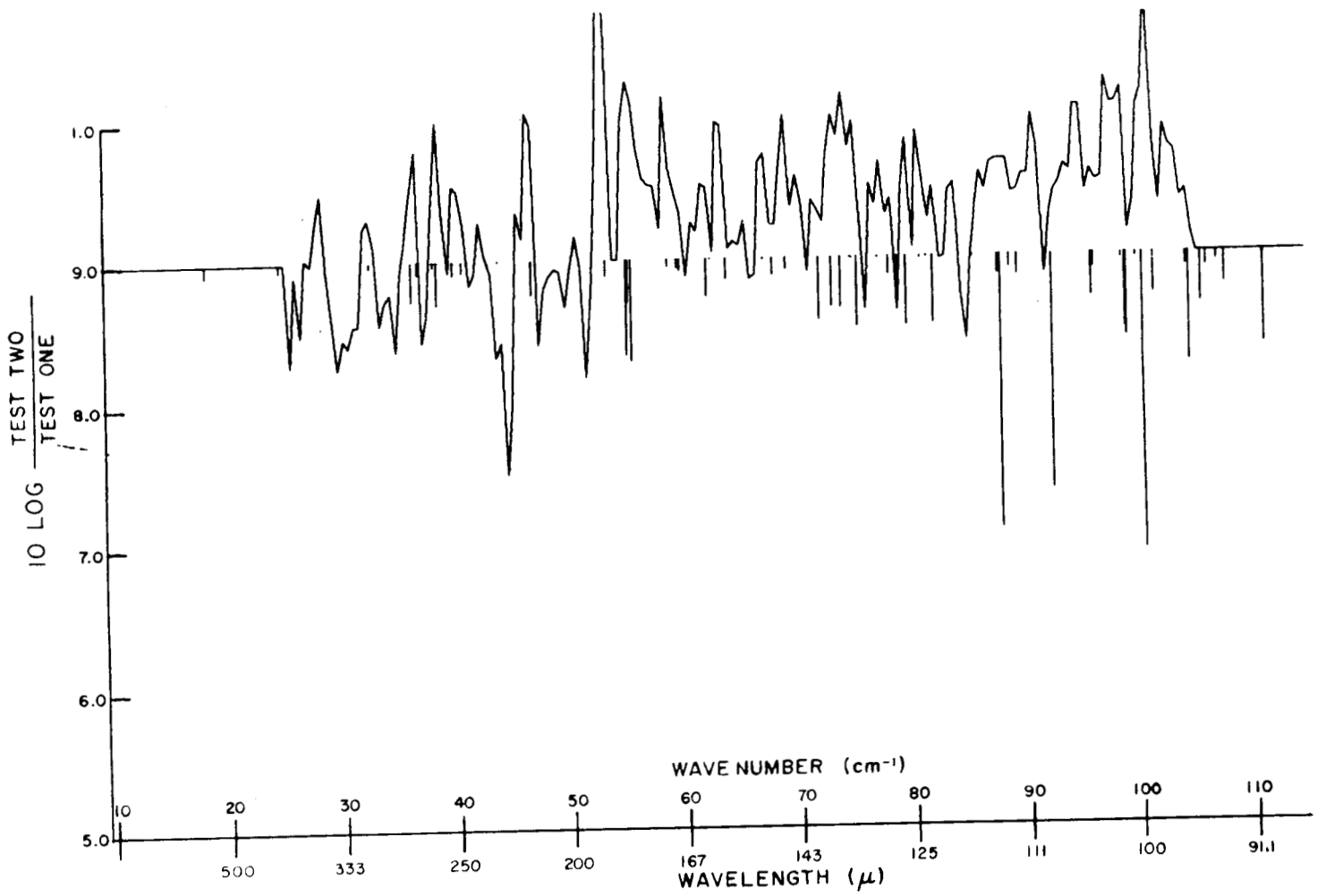

Fig. 23. The plot of the db loss of Fig. 21. Absorption is plotted upwards.

REFERENCES

1. VanVleck, "The Absorption of Microwave by Oxygen," Phys. Rev. 71, pp. 413 (1947).

2. Randall, H. M., Dennison, D. M., Ginsburg, N., and Weber, L. R., "The Far Infrared Spectrum of Water Vapor," Phys. Rev. 52, p. 163 (1937).

3. Michelson, A. A., "On the Application of Interference Methods to Spectroscopic Measurements," Phil. Mag., v31, 338, and v34, 280 and 407 (1892).

4. Fellget, P., Doctorial thesis, Cambridge University, England (1958).

5. Low, F. J., "Low-temperature Germanium Bolometer," J. Opt. Soc. Am., v51, 1300 (1961).

6. Wang, S. C., "On the Asymmetric Top in Quantum Mechanics," Phys. Rev. 34, pp. 243 (1929).

7. Kramers, H. A. and Ittmann, G. P., "Fur Quantelung des Asymmetrischen Kreisels I," Z. Phys. 53, p. 553 (1929).

8. Kramers, H. A. and Ittmann, G. P., "Zur Quantelung des Asymmetrischen Kreisels II," Z. Phys. 58, p. 217 (1929).

9. Kramers, H. A. and Ittmann, G. P., "Zur Quantelung des Asymmetrischen Kreisels III," Z. Phys. 60, p. 663 (1930).

10. Dennison, D. M., "The Infrared Spectra of Polyatomic Molecules," Rev. Mod. Phys. 3, p. 280 (1931).

11. Nielsen, H. H., "Infrared Bands of Slightly Asymmetric Molecules," Phys. Rev. 38, p. 1432 (1931).

12. King, G. W., Hainer, R. M., and Cross, P. C., "The Asymmetric Rotor," J. Chem. Phys. 11, pp. 27-42 (1943).

13. Schwendeman, R. H., "Table of Coefficients for the Energy of Levels of a Near Symmetric Top," J. Chem. Phys. 27, p. 986 (1957).

14. Polo, S. R., "Energy Levels of Slightly Asymmetric Top Molecules," Canadian J. Physc., 35, p. 880 (1957).

15. Brown, L. C. and Parker, P. M., "Computation of Rigid Asymmetric Rotator Constants from Energy Moments," J. Chem. Phys., v27, p. 1109 (1957).

16. Baker, J. G., "Energy Levels of an Asymmetric Rotor," Phys. Rev., v110, p. 282 (1958).

17. Long, R. K., "Absorption of Laser Radiation in the Atmosphere," Report 1579-3, 31 May 1963, Antenna Laboratory, The Ohio State University Research Foundation; prepared under Contract AF 33(657)-10824 for Air Force Avionics Laboratory, Research and Technology Division, Wright-Patterson Air Force Base, Ohio. (AD 410 571)

18. Williams, R. A., "An Interferometric Receiver for Submillimeter Radiometry," Report 1093-25, 1 February 1965, Antenna Laboratory, The Ohio State University Research Foundation; prepared under Grant Number NsG-74-60 for National Aeronautics and Space Administration.

19. Spanbauer, R. L., "Development and Use of a Carbon Furnace as a High Intensity Source of Infrared Radiations," Master's thesis, The Ohio State University, 1964.

20. Townes, C. H. and Schawlow, A. L., Microwave Spectroscopy, McGraw-Hill Book Co., 1955.